Engineering with Computers (2022) 38 (Suppl 5):S3725–S3741
https://doi.org/10.1007/s00366-020-01200-x

ORIGINAL ARTICLE

Frequency simulation of viscoelastic multi-phase reinforced fully symmetric systems

M. S. H. Al-Furjan[1,2] · Mostafa Habibi[3,4] · Jing Ni[1] · Dong won Jung[5] · Abdelouahed Tounsi[6]

Received: 27 July 2020 / Accepted: 8 October 2020 / Published online: 27 October 2020

Abstract

Honeycomb structures have the geometry of the lattice network to allow the minimization of the amount of used material to reach minimal material cost and minimal weight. In this regard, this article deals with the frequency analysis of imperfect honeycomb core sandwich disk with multiscale hybrid nanocomposite (MHC) face sheets rested on an elastic foundation. The honeycomb core is made of aluminum due to its low weight and high stiffness. The rule of the mixture and modified Halpin–Tsai model are engaged to provide the effective material constant of the composite layers. By employing Hamilton's principle, the governing equations of the structure are derived and solved with the aid of the generalized differential quadrature method (GDQM). Afterward, a parametric study is done to present the effects of the orientation of fibers (θ_f/π) in the epoxy matrix, Winkler–Pasternak constants (K_w and K_p), thickness to length ratio of the honeycomb network (t_h/l_h), the weight fraction of CNTs, value fraction of carbon fibers, angle of honeycomb networks, and inner to outer radius ratio on the frequency of the sandwich disk. The results show that it is true that the roles of K_w and K_p are the same as an enhancement, but the impact of K_w could be much more considerable than the effect of K_p on the stability of the structure. Additionally, when the angle of the fibers is close to the horizon, the frequency of the system improves.

Keywords Sandwich disk · Honeycomb core · Elastic foundation · GDQM · Imperfection multiscale hybrid laminated nanocomposite · Frequency characteristic

✉ Mostafa Habibi
mostafahabibi@duytan.edu.vn

✉ Dong won Jung
jdwcheju@jejunu.ac.kr

✉ Abdelouahed Tounsi
tou_abdel@yahoo.com

M. S. H. Al-Furjan
Rayan@hdu.edu.cn

Jing Ni
Jing.ni20@163.com

1 School of Mechanical Engineering, Hangzhou Dianzi University, Hangzhou 310018, China

2 State Key Laboratory of Silicon Materials, School of Materials Science and Engineering, Zhejiang University, Hangzhou 310027, China

3 Institute of Research and Development, Duy Tan University, Da Nang 550000, Vietnam

4 Faculty of Electrical-Electronic Engineering, Duy Tan University, Da Nang 550000, Vietnam

5 Departement of Mechanical Engineering, Jeju National University, Jeju 690-756, South Korea

6 Yonsei Frontier Lab, Yonsei University, Seoul, South Korea

List of symbols

h, R_i, and R_o	Thickness, the inner and outer radius of the disk, respectively
CNTs	Carbon nanotubes
F and NCM	Fiber and nanocomposite matrix, respectively
ρ, E, ν and G	The density, Young's modulus, Poisson's ratio, and shear parameter, respectively
V_{NCM}, V_F	Volume fractions of the nanocomposite matrix and fiber, respectively
l^{CNT}, t^{CNT}, d^{CNT}, E^{CNT} and V_{CNT}	The length, thickness, diameter, Young's modulus, and volume fraction of carbon nanotubes, respectively
V^*_{CNT}, W_{CNT}	Effective volume fraction and weight fraction of the CNTs, respectively

Nt, V_{CNT}	Layer number and volume fraction of CNTs
E_1^* and E_2^*	Young's modulus in R and θ directions, respectively
v_{12}^* and v_{21}^*	Poisson's ratio in R and θ directions, respectively
G_{12}^*	In-plane shear modulus
E_S and ρ_S	Young's modulus and mass density of the base material, which is aluminum for the honeycomb core, respectively
t_m, h_H, l_m, and θ_h	The cell wall thickness, the sides of the hexagonal cell, and the angle of honeycomb core, respectively
U, V, W	Displacement fields of a disk
u, v, w, u_1, and v_1	The displacements of the mid-surface of the disk
ε_{RR} and $\varepsilon_{\theta\theta}$	The corresponding normal strains in R and θ directions, respectively
γ_{RZ}, $\gamma_{R\theta}$ and $\gamma_{\theta Z}$	The shear strain in the R–Z, R–θ and θ–Z plane
U^*, T^*, and W^*	Corresponding strain energy of the system, kinetic energy of the system, and the work done, respectively
Q_{ij} and $\overline{Q}_{ij}$	Stiffness elements, stiffness elements related to orientation angle, and the orientation angle, respectively
θ_f	The lamination angle concerning the disk R axis
K_W and K_P	Winkler and Pasternak foundation coefficient
N_r and N_θ	The number of grid points along the radial and circumferential directions, respectively
d, b, and δ	d As a subscript stands for the domain grid points, b as a subscript stands for boundary grid points and the displacement vector, respectively
M_{ij} and K_{ij}	Components of mass and stiffness matrices, respectively
$M_{ij}{}^*$ and $K_{ij}{}^*$	Components of mass and stiffness matrices in the GDQ method, respectively
ω_n and $\overline{\omega}_n$	Dimensional and non-dimensional value of natural frequency

1 Introduction

As a matter of fact, as well as improving the properties of the applicable structures [1, 2] in the different engineering fields [3–5] by employing the various methods in the last decades, researchers have found a novel and excellent method for enhancing the static and dynamic responses of the low-density plate, beam, shell, and disk [6–12]. Based on this matter, honeycombed structures are presented for use in the related industry. Mukhopadhyay et al. [13]. investigated the vibrational characteristics of the sandwich panel with honeycomb core with the aid of Hamilton's principle. They reported that the honeycomb core could improve the natural frequency and, finally, the stiffness of the sandwich panel. Ref. [14] studied the effects of various defects that occur for building honeycomb composite beams and obtained the mechanical performance of honeycomb beams in different vibration modes using finite element analysis and fast Fourier transform analyzer. Significant results of this study showed that the natural frequency of the structure decreases with increasing defect percentage. Mozafari et al. [15] studied the vibrational frequencies of honeycomb sandwich panels with different cores. Using experimental testing, they determined the mechanical properties of polyurethane foams. They examined the effect of the first resonant frequency, the shape of the state, and the impact of the foams on the vibrational response of the core. The free vibration of the graded corrugated lattice core structure and the analytical method to solve the governing equations were examined by Ref. [16]. They analyzed the effect of beam length, graded parameters, and facial leaf thickness on the frequency responses of the mentioned structure. Amini et al. [17] controlled the amplitude of the vibrations of a solar panel that is made of a honeycomb core and smart layers. With Hamilton's principle and thin plate theory, they developed the motion equations and boundary conditions. Finally, they found that the elastoelectric effects have an essential role in the frequency responses of the solar panel. Ref [18]. evaluated the post-buckling behavior of panels with honeycomb cores and reinforced by graphene particles. The researchers' findings show that core thickness, GPL weight fraction, and geometric parameters related to the panel have an essential role in the post-buckling behavior of the sandwich panel. The bending behavior of a curved beam with graphene nanoplatelets and honeycomb core was studied by Sobhy [19]. Using DQM, they solved the complex motion equations and associated boundary conditions. Wang et al. [20] conducted research about frequency responses of a sandwich panel with honeycomb core using experimental and finite element outcomes. Finally, their essential work found that the thickness ratio of the face sheet and filling foam density had a vital role in the frequency of the sandwich panel with a honeycomb core. Ref [21]. presented a frequency analysis of a sandwich beam with honeycomb hybrid core with the aid of finite element and experimental techniques. Nonlinear frequency responses of a honeycomb sandwich shell were presented by Zhang et al. [22]. They solved the governing equations of the structure with simply supported boundary conditions via the homotopy perturbation method. In recent years, the use of CNTs as reinforcement has got a lot of attention. For this issue, Keleshteri et al. [23] analyzed major bending responses of an FG annular plate, which is enhanced through employing CNTs and surrounded by an elastic foundation. They believe that in their mathematical approach, the von Karman and thick shear deformation models are utilized for reporting more accuracy when it comes to presenting results. Furthermore, to solve the equations obtained via energy methods, they employed the GDQ model along with Newton–Raphson. Their emphasized outcome is that the thickness and the value fraction of CNT may play a prominent role when it comes to the investigation of the annular disk's nonlinear frequency. Ansari and Torabi [24] analyzed nonlinear forced and free dynamics of an FG disk by using the von Kármán method as well as thin SDT. They mainly emphasized the modified GDQ model to solve the FG disk's governing equation and reported a structure's large amplitude vibration. Keleshteri et al. [25, 26] conducted a study on the frequency of the CNT-reinforced circular sector plate considering a piezoelectric layer utilizing GDQM and FSDT. By taking into account the same process, Keleshtary et al. [27] investigated the FG-CNT reinforced circular plate's amplitude performance covered by the piezoelectric layer and sitting on an elastic medium. Torabi and Ansari [28] reported that it is essential to extend motion equations of the FG-CNT reinforced circular plate's large amplitude vibration based on the relations of general asymmetry in the existence of primary thermal stress for achieving accurate results. Also, many studies reported the application of applied soft computing method for prediction of the behavior of the complex system [29–36].

Vinyas and Harursampath [37] performed geometrically nonlinear free vibration behaviour of higher-order shear deformable carbon nanotube-reinforced magneto-electro-elastic doubly curved shells. Dat et al. [38] presented an analytical approach on the nonlinear magneto-electro-elastic vibration of a smart sandwich plate. They modeled the sandwich plate consisting of a carbon nanotube-reinforced nanocomposite core integrated with two magneto-electro-elastic face sheets. Mahesh and Harursampath [39, 40] investigated the nonlinear deflection problem of magneto-electro-elastic shells reinforced with carbon nanotubes subjected to multiphysics loads such as mechanical, electric and magnetic loads. In this regard, they derived a mathematical model based on higher-order shell theory, von Karman's nonlinearity using finite element platform. Vinyas [41] explored the vibrational behavior of porous functionally graded magneto-electro-elastic circular and annular plates through finite element procedures.

Based on the extremely detailed exploration in the literature by the authors, no one can claim there is a research on the frequency analysis of the sandwich disk with a honeycomb core and imperfect MHLC face sheets rested on an elastic foundation. First-order shear deformation theory (FSDT) is applied to formulate the stresses–strains relation. Rule of the mixture and modified Halpin–Tsai model are engaged to provide the effective material constant of the MHC disk. By employing Hamilton's principle, the governing equations of the structure are derived. Finally, the outcomes of the presented study show that some geometrical and physical parameters have an important role in the frequency responses of the sandwich disk.

2 Mathematical modeling

2.1 The homogenization process of MHC

The procedure of homogenization is made of two main steps based upon the Halpin–Tsai model, together with a micromechanical theory [6–12, 42]. The first stage is engaged with computing the effective characteristics of the composite reinforced with CF as follows [43]:

$$E_{11} = V_F E_{11}^F + V_{NCM} E^{NCM}, \tag{1}$$

$$\frac{1}{E_{22}} = \frac{V_f}{E_{22}^F} + \frac{V_{NCM}}{E^{NCM}} - V_F V_{NCM} \times \frac{\left(\nu^F\right)^2 \frac{E^{NCM}}{E_{22}^F} + \left(\nu^{NCM}\right)^2 \frac{E_{22}^F}{E^M} - 2\nu^F \nu^{NCM}}{V_F E_{22}^F + V_{NCM} E^{NCM}}, \tag{2}$$

$$\frac{1}{G_{12}}=\frac{V_{\mathrm{F}}}{G_{12}^{\mathrm{F}}}+\frac{V_{\mathrm{NCM}}}{G^{\mathrm{NCM}}}, \tag{3}$$

$$\rho=V_{\mathrm{NCM}}\rho^{\mathrm{NCM}}+V_{\mathrm{F}}\rho^{\mathrm{F}}, \tag{4}$$

$$v_{12}=V_{NCM}v^{NCM}+V_{F}v^{F}. \tag{5}$$

The volume fraction of the fiber and nanocomposite matrixes can be given by [43]:

$$V_{\mathrm{F}}+V_{\mathrm{NCM}}=1. \tag{6}$$

The second step is organized to obtain the effective characteristics of the nanocomposite matrix reinforced with CNTs with the aid of the extended Halpin–Tsai micromechanics as follows:

$$E^{\mathrm{NCM}}=E^{\mathrm{M}}\left(\frac{5}{8}\left(\frac{1+2\beta_{\mathrm{dd}}V_{\mathrm{CNT}}}{1-\beta_{\mathrm{dd}}V_{\mathrm{CNT}}}\right)+\frac{3}{8}\left(\frac{1+2\left(l^{\mathrm{CNT}}/d^{\mathrm{CNT}}\right)\beta_{\mathrm{dl}}V_{\mathrm{CNT}}}{1-\beta_{\mathrm{dl}}V_{\mathrm{CNT}}}\right)\right). \tag{7}$$

Here, β_{dd} and β_{dl} are computed as the following expression:

$$\beta_{\mathrm{dl}}=\frac{(E_{11}^{\mathrm{CNT}}/E^{\mathrm{M}})}{(l^{\mathrm{CNT}}/2t^{\mathrm{CNT}})+(E_{11}^{\mathrm{CNT}}/E^{\mathrm{M}})}-\frac{(d^{\mathrm{CNT}}/4t^{\mathrm{CNT}})}{(l^{\mathrm{CNT}}/2t^{CNT})+(E_{11}^{\mathrm{CNT}}/E^{\mathrm{M}})},$$
$$\beta_{\mathrm{dd}}=\frac{(E_{11}^{CNT}/E^{M})}{(d^{\mathrm{CNT}}/2t^{\mathrm{CNT}})+(E_{11}^{\mathrm{CNT}}/E^{M})}-\frac{(d^{\mathrm{CNT}}/4t^{CNT})}{(d^{CNT}/2t^{\mathrm{CNT}})+(E_{11}^{\mathrm{CNT}}/E^{\mathrm{M}})}. \tag{8}$$

The volume fraction of CNTs can be formulated as below [44–46]:

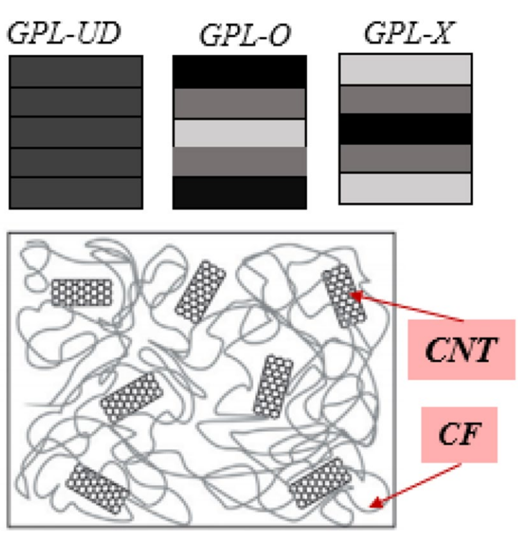

Fig. 1 Distribution of CNT and CF through the thickness of the MHL composite

$$V_{\mathrm{CNT}}^{*}=\frac{W_{\mathrm{CNT}}}{W_{\mathrm{CNT}}+\left(\frac{\rho^{\mathrm{CNT}}}{\rho^{\mathrm{M}}}\right)\left(1-W_{\mathrm{CNT}}\right)}. \tag{9}$$

Also, various kinds of MHC distribution along with thickness direction can be given by (see Fig. 1):

$$\begin{aligned}
&V_{\mathrm{CNT}}=4V_{\mathrm{CNT}}^{*}\frac{\left|\xi_{j}\right|}{h} \quad \mathrm{FG-X}\\
&V_{\mathrm{CNT}}=2V_{\mathrm{CNT}}^{*}\left(1-2\frac{\left|\xi_{j}\right|}{h}\right)\mathrm{FG-O}\\
&V_{\mathrm{CNT}}=V_{\mathrm{CNT}}^{*} \quad \mathrm{FG-UD}.
\end{aligned} \tag{10}$$

Here, $\xi_{j}=\left(\frac{1}{2}+\frac{1}{2N_{t}}-\frac{j}{N_{t}}\right)h \quad j=1,2,\ldots,N_{t}$.

Furthermore, the sum of V_{M} and V_{CNT} is equal to one as follows [6–12, 42]:

$$V_{\mathrm{CNT}}+V_{\mathrm{M}}=1. \tag{11}$$

Finally, the mechanical properties of the MHC face sheets can be given by [44–46]:

$$\rho^{\mathrm{NCM}}=V_{\mathrm{CNT}}\rho^{\mathrm{CNT}}+V_{\mathrm{M}}\rho^{\mathrm{M}}, \tag{12}$$

$$v^{\mathrm{NCM}}=v^{\mathrm{M}}, \tag{13}$$

$$G^{\mathrm{NCM}}=\frac{E^{\mathrm{NCM}}}{2\left(1+v^{\mathrm{NCM}}\right)}. \tag{14}$$

In Fig. 2, various kinds of porosity distributions, namely, uniform, X, and O, are presented. The Young's modulus, shear modulus, and mass density are as below:

$$\tilde{E}_{11}=E_{11}\left(1-e_{0}s(z)\right), \tag{15a}$$

$$\tilde{E}_{22}=E_{22}\left(1-e_{0}s(z)\right), \tag{15b}$$

$$\tilde{G}_{12}(z)=\frac{\tilde{E}_{11}}{2(1-v(z))}, \tag{15c}$$

$$\tilde{\rho}(z)=\rho(z)\left[1-e_{\mathrm{m}}s(z)\right]+V_{\mathrm{ncm}}\rho_{\mathrm{ncm}}, \tag{15d}$$

where:

$$s=\begin{cases} s_{\mathrm{o}} & \mathrm{PD-UD}\\ s_{\mathrm{o}}\cos\left(\frac{\pi}{4}+\frac{\pi z}{2h}\right) & \mathrm{PD-X}\\ s_{\mathrm{o}}\cos\left(\frac{\pi z}{h}\right) & \mathrm{PD-O}\end{cases} \tag{16}$$

Based on the Gaussian random field scheme, we have:

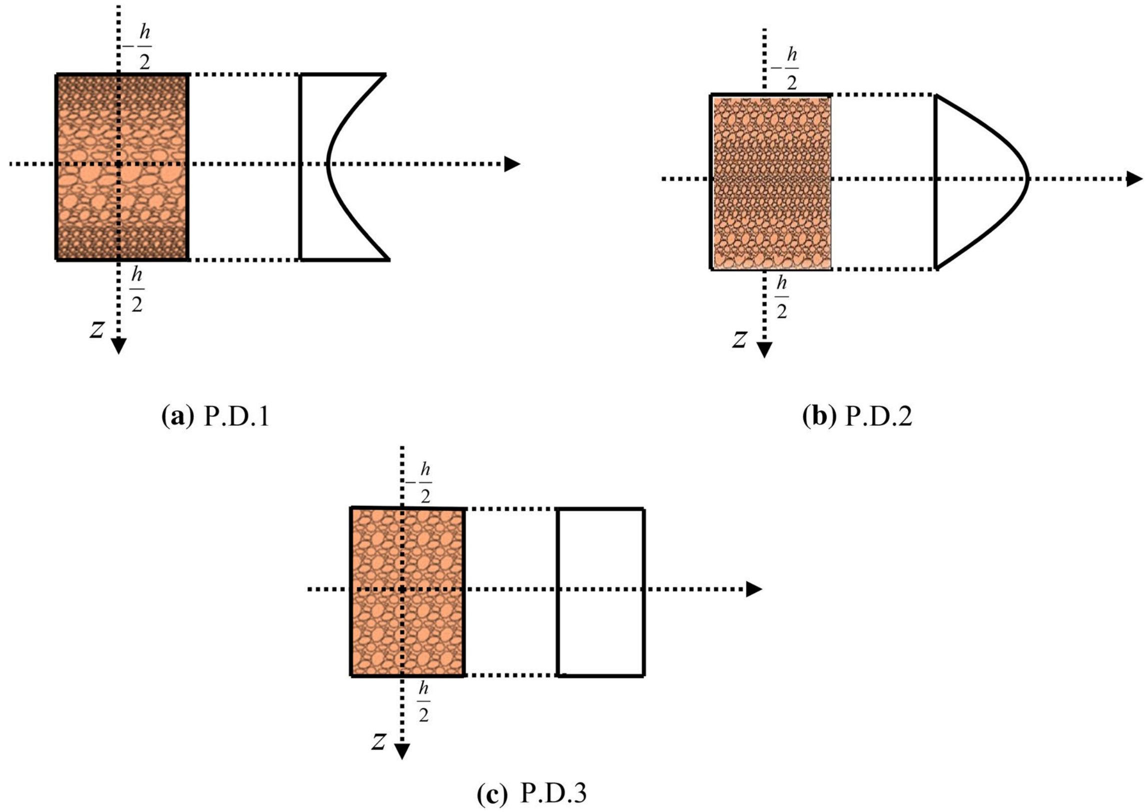

Fig. 2 Patterns of porosity distribution through the thickness of MHC

$$e_{\mathrm{m}} = \frac{1.121\left[1-\left(1-e_0 s(z)\right)^{\frac{1}{2.3}}\right]}{s(z)}. \tag{17}$$

The Poisson's ratio of the porous disk corresponding to the closed-cell Gaussian random field can be written as:

$$\begin{aligned}\tilde{v}_{12} =& 0.221\left(1-\frac{\tilde{\rho}(z)}{\rho}\right) \\ &+ v_{12}\left[1+0.342\left(1-\frac{\tilde{\rho}(z)}{\rho}\right)^2 - 1.21\left(1-\frac{\tilde{\rho}(z)}{\rho}\right)\right],\end{aligned} \tag{18a}$$

$$\tilde{v}_{21} = \tilde{v}_{12}\frac{\tilde{E}_{11}}{\tilde{E}_{22}}. \tag{18b}$$

Also, when the total masses of the disk with different porosity distributions are the same, the value of S_0 can be formulated as:

$$s_0 = \frac{1}{e_0}\left[1-\left(\frac{\frac{1}{h}\int_{-\frac{h}{2}}^{\frac{h}{2}}\frac{\tilde{\rho}(z)}{\rho}\mathrm{d}z + 0.121}{1.121}\right)^{2.3}\right]. \tag{19}$$

2.2 Modeling of honeycomb cores

The hexagonal cell geometry is illustrated in Fig. 3. According to the Gibson model, we have [47]:

$$E_{11}^{*} = \frac{\sigma_1}{\varepsilon_1} = E_{\mathrm{S}}\left(\frac{t}{l}\right)\frac{\cos\left(\theta_{\mathrm{h}}\right)}{\left(h/1+\sin\left(\theta_{\mathrm{h}}\right)\right)\sin^2\left(\theta_{\mathrm{h}}\right)}\frac{1}{1+(t/1)^2\cot^2\left(\theta_{\mathrm{h}}\right)}, \tag{20-a}$$

$$E_{22}^{*} = \frac{\sigma_2}{\varepsilon_2} = E_{\mathrm{S}}\left(\frac{t}{l}\right)^3\frac{\left(h/1+\sin\left(\theta_{\mathrm{h}}\right)\right)}{\cos^3\left(\theta_{\mathrm{h}}\right)}\frac{1}{1+(t/1)^2\cot^2\left(\theta_{\mathrm{h}}\right)}, \tag{20-b}$$

$$v_{12}^{*} = -\frac{\varepsilon_2}{\varepsilon_1} = \frac{\cos^2\left(\theta_{\mathrm{h}}\right)}{\left(h/1+\sin\left(\theta_{\mathrm{h}}\right)\right)\sin\left(\theta_{\mathrm{h}}\right)}\frac{1-(t/1)^2}{1+\cot^2\left(\theta_{\mathrm{h}}\right)(t/1)^2}, \tag{20-c}$$

$$\begin{aligned}v_{21}^{*} &= -\frac{\varepsilon_1}{\varepsilon_2} \\ &= \frac{\left(h/1+\sin\left(\theta_{\mathrm{h}}\right)\right)\sin\left(\theta_{\mathrm{h}}\right)}{\cos^2\left(\theta_{\mathrm{h}}\right)}\cdot\frac{1-(t/1)^2}{1+\left((h/1)\sec^2\left(\theta_{\mathrm{h}}\right)+\tan^2\left(\theta_{\mathrm{h}}\right)\right)(t/1)^2},\end{aligned} \tag{20-d}$$

$$G_{12}^{*} = E_{\mathrm{S}}\left(\frac{t}{l}\right)^3\frac{\left(h/1+\sin\left(\theta_{\mathrm{h}}\right)\right)}{(h/1)^2\cos\left(\theta_{\mathrm{h}}\right)}\frac{1}{R} \tag{20-e}$$

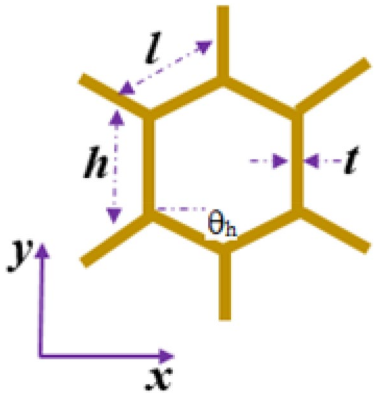

Fig. 3 The hexagonal cell geometry

$$R=\left(1+2\frac{h}{l}+\left(\frac{t}{l}\right)^{2}\frac{h/1+\sin\left(\theta_{\mathrm{h}}\right)}{(h/1)^{2}}\left[\left(h/1+\sin\left(\theta_{\mathrm{h}}\right)\right)\tan^{2}\left(\theta_{\mathrm{h}}\right)+\sin\left(\theta_{\mathrm{h}}\right)\right]\right), \tag{20-f}$$

$$\frac{\rho^{*}}{\rho_{S}}=\frac{\left(\frac{t}{l}\right)\left(\frac{h}{l}+2\right)}{2\cos\left(\theta_{\mathrm{h}}\right)\left(\frac{h}{l}+\sin\left(\theta_{\mathrm{h}}\right)\right)}. \tag{20-i}$$

Figure 4 is presented for the geometry of the imperfect honeycomb core sandwich disk with MHC face sheets.

Based on FSDT, the displacement fields can be defined by the below relations [48–50]:

$$\begin{aligned}u^{\eta}&=u_{0}^{\eta}+zu_{1}^{\eta}\\ v^{\eta}&=v_{0}^{\eta}+zv_{1}^{\eta}\\ w^{\eta}&=w_{0}^{\eta}.\end{aligned} \tag{21}$$

In Eq. (21), η defines the core, top, and bottom layers.

2.3 Strain–stress of the honeycomb core

Based on FSDT, the strain–stress formulation can be written as [44–46, 48–57]:

$$\begin{bmatrix}\sigma_{RR}\\ \sigma_{\theta\theta}\\ \sigma_{R\theta}\\ \sigma_{Rz}\\ \sigma_{\theta z}\end{bmatrix}^{c}=\begin{bmatrix}Q_{11}&Q_{12}&0&0&0\\ Q_{12}&Q_{22}&0&0&0\\ 0&0&Q_{66}&0&0\\ 0&0&0&Q_{55}&0\\ 0&0&0&0&Q_{44}\end{bmatrix}^{c}\begin{bmatrix}\varepsilon_{RR}\\ \varepsilon_{\theta\theta}\\ \varepsilon_{R\theta}\\ \varepsilon_{Rz}\\ \varepsilon_{\theta z}\end{bmatrix}^{c}$$

$$Q_{11}^{c}=\frac{E_{11}^{*}}{1-v_{12}^{*}v_{21}^{*}},\quad Q_{22}^{c}=\frac{E_{22}^{*}}{1-v_{12}^{*}v_{21}^{*}},\quad Q_{12}^{c}=\frac{v_{21}^{*}E_{22}^{*}}{1-v_{12}^{*}v_{21}^{*}},$$
$$Q_{44}^{c}=G_{12}^{*},\ Q_{55}^{c}=G_{13}^{*},\ Q_{66}^{c}=G_{23}^{*},\ G_{13}^{*}=G_{23}^{*}=G_{12}^{*}. \tag{22}$$

So, the strain components would be written as:

$$\begin{Bmatrix}\varepsilon_{RR}\\ \varepsilon_{\theta\theta}\\ \gamma_{R\theta}\\ \gamma_{Rz}\\ \gamma_{\theta z}\end{Bmatrix}^{\psi}=\begin{Bmatrix}\varepsilon_{RR}^{0}\\ \varepsilon_{\theta\theta}^{0}\\ \gamma_{R\theta}^{0}\\ \gamma_{Rz}^{0}\\ \gamma_{\theta z}^{0}\end{Bmatrix}^{\psi}+z\begin{Bmatrix}\kappa_{RR}\\ \kappa_{\theta\theta}\\ \kappa_{R\theta}\\ \kappa_{Rz}\\ \kappa_{\theta z}\end{Bmatrix}^{\psi} \tag{23a}$$

Fig. 4 The geometry of honeycomb core sandwich disk with MHC face sheet

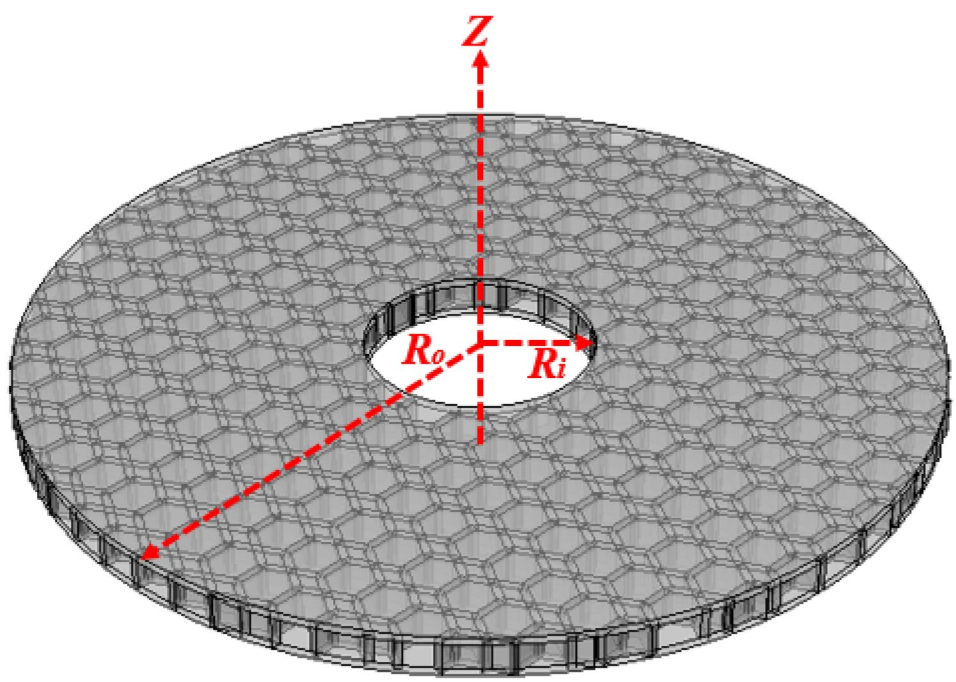

$$\begin{Bmatrix}\varepsilon_{RR}^0\\ \varepsilon_{\theta\theta}^0\\ \gamma_{R\theta}^0\\ \gamma_{Rz}^0\\ \gamma_{\theta z}^0\end{Bmatrix}^{c}=\begin{Bmatrix}\frac{\partial u}{\partial R}\\ \frac{u}{R}+\frac{\partial v}{R\partial\theta}\\ \frac{\partial u}{R\partial\theta}+\frac{\partial v}{\partial R}-\frac{v}{R}\\ \phi_R+\frac{\partial w}{\partial R}\\ \phi_\theta+\frac{\partial w}{R\partial\theta}\end{Bmatrix}^{c},\quad \begin{Bmatrix}\kappa_{RR}\\ \kappa_{\theta\theta}\\ \kappa_{R\theta}\\ \kappa_{Rz}\\ \kappa_{\theta z}\end{Bmatrix}^{c}=\begin{Bmatrix}\frac{\partial\phi_R}{\partial R}\\ \frac{\phi_R}{R}+\frac{\partial\phi_\theta}{R\partial\theta}\\ \frac{\partial\phi_R}{R\partial\theta}+\frac{\partial\phi_\theta}{\partial R}-\frac{\phi_\theta}{R}\\ 0\\ 0\end{Bmatrix}^{c}. \tag{23b}$$

Stress–strain relations of MHC angle-ply-laminated disk can be written as follows [58–65]:

$$\begin{bmatrix}\sigma_{RR}\\ \sigma_{\theta\theta}\\ \sigma_{R\theta}\\ \sigma_{Rz}\\ \sigma_{\theta z}\end{bmatrix}^{\psi}=\begin{bmatrix}\hat{\bar{Q}}_{11}&\hat{\bar{Q}}_{12}&0&0&\hat{\bar{Q}}_{16}\\ \hat{\bar{Q}}_{21}&\hat{\bar{Q}}_{22}&0&0&\hat{\bar{Q}}_{26}\\ 0&0&\hat{\bar{Q}}_{44}&\hat{\bar{Q}}_{45}&0\\ 0&0&\hat{\bar{Q}}_{45}&\hat{\bar{Q}}_{55}&0\\ \hat{\bar{Q}}_{16}&\hat{\bar{Q}}_{26}&0&0&\hat{\bar{Q}}_{66}\end{bmatrix}^{\psi}\begin{bmatrix}\varepsilon_{RR}\\ \varepsilon_{\theta\theta}\\ \varepsilon_{R\theta}\\ \varepsilon_{Rz}\\ \varepsilon_{\theta z}\end{bmatrix}^{\psi}. \tag{24}$$

The above equation ψ defines the top and bottom layers, where

$$\hat{\bar{Q}}_{11}^{\psi}=\cos^4\theta_{\mathrm{f}}\tilde{Q}_{11}^{\psi}+2\sin^2\theta_{\mathrm{f}}\cos^2\theta_{\mathrm{f}}\left(\tilde{Q}_{12}^{\psi}+2\tilde{Q}_{66}^{\psi}\right)+\sin^4\theta_{\mathrm{f}}\tilde{Q}_{22}^{\psi}, \tag{25a}$$

$$\hat{\bar{Q}}_{12}^{\psi}=\sin^2\theta_{\mathrm{f}}\cos^2\theta_{\mathrm{f}}\left(\tilde{Q}_{11}^{\psi}+\tilde{Q}_{22}^{\psi}-4\tilde{Q}_{66}^{\psi}\right)+\left(\sin^4\theta_{\mathrm{f}}+\cos^4\theta_{\mathrm{f}}\right)\tilde{Q}_{12}^{\psi}, \tag{25b}$$

$$\hat{\bar{Q}}_{16}^{\psi}=\cos^3\theta_{\mathrm{f}}\sin\theta_{\mathrm{f}}\left(2\tilde{Q}_{11}^{\psi}-2\tilde{Q}_{12}^{\psi}-\tilde{Q}_{66}^{\psi}\right)+\cos\theta_{\mathrm{f}}\sin^3\theta_{\mathrm{f}}\left(\tilde{Q}_{66}^{\psi}+2\tilde{Q}_{12}^{\psi}-2\tilde{Q}_{22}^{\psi}\right), \tag{25c}$$

$$\hat{\bar{Q}}_{22}^{\psi}=\sin^4\theta_{\mathrm{f}}\tilde{Q}_{11}^{\psi}+2\sin^2\theta_{\mathrm{f}}\cos^2\theta_{\mathrm{f}}\tilde{Q}_{12}^{\psi}+\cos^4\theta_{\mathrm{f}}\tilde{Q}_{22}^{\psi}+2\sin^2\theta_{\mathrm{f}}\cos^2\theta_{\mathrm{f}}\left(\tilde{Q}_{12}^{\psi}+2\tilde{Q}_{66}^{\psi}\right), \tag{25d}$$

$$\hat{\bar{Q}}_{26}^{\psi}=\cos^3\theta_{\mathrm{f}}\sin\theta_{\mathrm{f}}\left(2\tilde{Q}_{12}^{\psi}-2\tilde{Q}_{22}^{\psi}+\tilde{Q}_{66}^{\psi}\right)+\cos\theta_{\mathrm{f}}\sin^3\theta_{\mathrm{f}}\left(2\tilde{Q}_{11}^{\psi}-2\tilde{Q}_{12}^{\psi}-\tilde{Q}_{66}^{\psi}\right), \tag{25e}$$

$$\hat{\bar{Q}}_{44}^{\psi}=\cos^2\theta_{\mathrm{f}}\tilde{Q}_{44}^{\psi}+\sin^2\theta_{\mathrm{f}}\tilde{Q}_{55}^{\psi}, \tag{25f}$$

$$\hat{\bar{Q}}_{45}^{\psi}=\cos\theta_{\mathrm{f}}\sin\theta_{\mathrm{f}}\left(\tilde{Q}_{55}^{\psi}-\tilde{Q}_{44}^{\psi}\right), \tag{25g}$$

$$\hat{\bar{Q}}_{55}^{\psi}=\cos^2\theta_{\mathrm{f}}\tilde{Q}_{55}^{\psi}+\sin^2\theta_{\mathrm{f}}\tilde{Q}_{44}^{\psi}, \tag{25h}$$

$$\hat{\bar{Q}}_{66}^{\psi}=\tilde{Q}_{66}^{\psi}\left(\cos^2\theta_{\mathrm{f}}-\sin^2\theta_{\mathrm{f}}\right)^2+4\sin^2\theta_{\mathrm{f}}\cos^2\theta_{\mathrm{f}}\left(\tilde{Q}_{11}^{\psi}+\tilde{Q}_{22}^{\psi}-2\tilde{Q}_{12}^{\psi}\right). \tag{25i}$$

The terms involved in Eq. (25) would be obtained as [45, 66–76]

$$\tilde{Q}_{11}^{\psi}=\frac{\tilde{E}_{11}}{1-\tilde{\nu}_{12}\tilde{\nu}_{21}},\ \tilde{Q}_{12}^{\psi}=\frac{\tilde{\nu}_{12}\tilde{E}_{22}}{1-\tilde{\nu}_{12}\tilde{\nu}_{21}},$$
$$\tilde{Q}_{22}^{\psi}=\frac{\tilde{E}_{22}}{1-\tilde{\nu}_{12}\tilde{\nu}_{21}},\ \tilde{Q}_{44}^{\psi}=\tilde{G}_{12},\ \tilde{Q}_{55}^{\psi}=\tilde{G}_{23},\ \tilde{Q}_{66}^{\psi}=\tilde{G}_{13}.$$

So, the strain components would be written as:

$$\begin{Bmatrix}\varepsilon_{RR}\\ \varepsilon_{\theta\theta}\\ \gamma_{R\theta}\\ \gamma_{Rz}\\ \gamma_{\theta z}\end{Bmatrix}^{\psi}=\begin{Bmatrix}\varepsilon_{RR}^0\\ \varepsilon_{\theta\theta}^0\\ \gamma_{R\theta}^0\\ \gamma_{Rz}^0\\ \gamma_{\theta z}^0\end{Bmatrix}^{\psi}+z\begin{Bmatrix}\kappa_{RR}\\ \kappa_{\theta\theta}\\ \kappa_{R\theta}\\ \kappa_{Rz}\\ \kappa_{\theta z}\end{Bmatrix}^{\psi} \tag{26}$$

Equation (26) can be rewritten as

$$\begin{Bmatrix}\varepsilon_{RR}^0\\ \varepsilon_{\theta\theta}^0\\ \gamma_{R\theta}^0\\ \gamma_{Rz}^0\\ \gamma_{\theta z}^0\end{Bmatrix}^{\psi}=\begin{Bmatrix}\frac{\partial u}{\partial R}\\ \frac{u}{R}+\frac{\partial v}{R\partial\theta}\\ \frac{\partial u}{R\partial\theta}+\frac{\partial v}{\partial R}-\frac{v}{R}\\ \phi_R+\frac{\partial w}{\partial R}\\ \phi_\theta+\frac{\partial w}{R\partial\theta}\end{Bmatrix}^{\psi},\quad \begin{Bmatrix}\kappa_{RR}\\ \kappa_{\theta\theta}\\ \kappa_{R\theta}\\ \kappa_{Rz}\\ \kappa_{\theta z}\end{Bmatrix}^{\psi}=\begin{Bmatrix}\frac{\partial\phi_R}{\partial R}\\ \frac{\phi_R}{R}+\frac{\partial\phi_\theta}{R\partial\theta}\\ \frac{\partial\phi_R}{R\partial\theta}+\frac{\partial\phi_\theta}{\partial R}-\frac{\phi_\theta}{R}\\ 0\\ 0\end{Bmatrix}^{\psi} \tag{27}$$

2.4 Compatibility equations

The compatibility conditions assuming perfect bonding between the core and the composite layers can be defined as follows [54, 58, 62, 77–84]:

$$\begin{aligned}&u^{\mathrm{c}}(z_{\mathrm{c}}=-h_{\mathrm{c}}/2)=u^{\mathrm{b}}(z_{\mathrm{b}}=h_{\mathrm{b}}/2),\\ &v^{\mathrm{c}}(z_{\mathrm{c}}=-h_{\mathrm{c}}/2)=v^{\mathrm{b}}(z_{\mathrm{b}}=h_{\mathrm{b}}/2),\\ &w^{\mathrm{c}}(z_{\mathrm{c}}=-h_{\mathrm{c}}/2)=w^{\mathrm{b}}(z_{\mathrm{p}}=h_{\mathrm{b}}/2),\\ &u^{\mathrm{c}}(z_{\mathrm{c}}=h_{\mathrm{c}}/2)=u^{\mathrm{t}}(z_{\mathrm{t}}=-h_{\mathrm{t}}/2),\\ &v^{\mathrm{c}}(z_{\mathrm{c}}=h_{\mathrm{c}}/2)=v^{\mathrm{t}}(z_{\mathrm{t}}=-h_{\mathrm{t}}/2),\\ &w^{\mathrm{c}}(z_{\mathrm{c}}=h_{\mathrm{c}}/2)=w^{\mathrm{t}}(z_{\mathrm{t}}=-h_{\mathrm{t}}/2).\end{aligned} \tag{28}$$

2.5 Extended Hamilton's principle

Based on energy methods known as the Hamilton principle, there are relations between boundary conditions and motion equations which can be written as [53–55, 85–90]:

$$\int_{t_1}^{t_2}\left(\delta T^*-\delta U^*+\delta W^*\right)^{\eta}\,\mathrm{d}t=0\,. \tag{29}$$

The corresponding kinetic energy of the rotating system would be formulated as [91–97]:

$$T^{*\eta}=\int_V\frac{1}{2}\rho^{\eta}\left[\left(\frac{\partial U}{\partial t}\right)^2+\left(\frac{\partial V}{\partial t}\right)^2+\left(\frac{\partial W}{\partial t}\right)^2\right]^{\eta}\mathrm{d}V, \tag{30}$$

$$\delta T^{*\eta} = \int_V \rho^\eta \left(\frac{\partial U}{\partial t}\frac{\partial \delta U}{\partial t} + \frac{\partial V}{\partial t}\frac{\partial \delta V}{\partial t} + \frac{\partial W}{\partial t}\frac{\partial \delta W}{\partial t} \right)^\eta \mathrm{d}V :$$

$$\delta T^{*\eta} = \int_{R_1}^{R_2}\int_0^{\theta} \begin{bmatrix} \left\{ -I_0\frac{\partial^2 u}{\partial t^2} - I_1\frac{\partial^2 \phi_R}{\partial t^2} \right\}\delta u + \left\{ -I_1\frac{\partial^2 u}{\partial t^2} - I_2\frac{\partial^2 \phi_R}{\partial t^{2u_1}} \right\}\delta\phi_R \\ + \left\{ -I_0\frac{\partial^2 v}{\partial t^2} - I_1\frac{\partial^2 \phi_\theta}{\partial t^2} \right\}\delta v + \left\{ -I_1\frac{\partial^2 v}{\partial t^2} - I_2\frac{\partial^2 \phi_\theta}{\partial t^2} \right\}\delta\phi_\theta \\ + \left\{ -I_0\frac{\partial^2 w}{\partial t^2} \right\}\delta w \end{bmatrix}^\eta R\mathrm{d}R\mathrm{d}\theta, \tag{31}$$

where:

$$\{I_i\} = \int_{-\frac{h}{2}}^{\frac{h}{2}} \rho^\eta(z)\{z^i\}dZ, \quad i = 0 : 6. \tag{32}$$

Also, the strain energy of the current composite structure would be obtained as:

$$\delta U^{*\eta} = \frac{1}{2}\iiint_V \sigma_{ij}^\eta \delta\varepsilon_{ij}^\eta \mathrm{d}V$$
$$= \int_A \begin{bmatrix} \left(N_{RR}\frac{\partial \delta u_0}{\partial R} + M_{RR}\frac{\partial \delta u_1}{\partial R} \right) + \begin{pmatrix} N_{\theta\theta}\frac{\partial \delta v_0}{R\partial\theta} + M_{\theta\theta}\frac{\partial \delta v_1}{R\partial\theta} \\ + N_{\theta\theta}\frac{\delta u_0}{R} + M_{\theta\theta}\frac{\delta u_1}{R} \end{pmatrix} \\ + \begin{pmatrix} N_{R\theta}\frac{\partial \delta v_0}{\partial R} + M_{R\theta}\frac{\partial \delta v_1}{\partial R} + N_{R\theta}\frac{\partial \delta u_0}{R\partial\theta} \\ + M_{R\theta}\frac{\partial \delta u_1}{R\partial\theta} - N_{R\theta}\frac{\delta v_0}{R} - M_{R\theta}\frac{\delta v_1}{R} \end{pmatrix} \\ + \left(N_{Rz}\left(\delta u_1 + \frac{\partial \delta w_0}{\partial R} \right) \right) + \left(N_{\theta z}\left(\delta v_1 + \frac{\partial \delta w_0}{R\partial\theta} \right) \right) \end{bmatrix}^\eta \mathrm{d}A, \tag{33}$$

where

$$\{N_{RR}, M_{RR}\}^\eta = \int_z \{\sigma_{RR}, z\sigma_{RR}\}^\eta \mathrm{d}z;$$
$$\{N_{\theta\theta}, M_{\theta\theta}\}^\eta = \int_z \{\sigma_{\theta\theta}, z\sigma_{\theta\theta}\}^\eta \mathrm{d}z;$$
$$\{N_{Rz}, M_{Rz}\}^\eta = \int_z \{\sigma_{Rz}, z\sigma_{Rz}\}^\eta \mathrm{d}z;. \tag{34}$$
$$\{N_{R\theta}, M_{R\theta}\}^\eta = \int_z \{\sigma_{R\theta}, z\sigma_{R\theta}\}^\eta \mathrm{d}z;$$
$$\{N_{\theta z}, M_{\theta z}\}^\eta = \int_z \{\sigma_{\theta z}, z\sigma_{\theta z}\}^\eta \mathrm{d}z.$$

Furthermore, the first variation of work done due to the elastic substrate can be formulated as follows:

$$\delta W^{*\eta} = \int \left(-K_w w\delta w + K_p\left[\left(\frac{\partial w}{\partial R} \right)\left(\frac{\partial}{\partial R}\delta w \right) + \frac{1}{R^2}\left(\frac{\partial w}{\partial \theta} \right)\left(\frac{\partial}{\partial \theta}\delta w \right) \right] \right)^\eta \mathrm{d}A. \tag{35}$$

Eventually, the governing equations and the corresponding boundary conditions can be derived by substituting Eqs. (35), (33), and (31) in Hamilton's principle (Eq. (29)) that can be given by the following equations:

$$\delta u_0^\eta : \frac{\partial}{\partial R}N_{RR}^\eta - \frac{N_{\theta\theta}^\eta - N_{RR}^\eta}{R} + \frac{\partial}{R\partial\theta}N_{R\theta}^\eta = I_0^\eta\frac{\partial^2 u_0^\eta}{\partial t^2} + I_1^\eta\frac{\partial^2 u_1^\eta}{\partial t^2}, \tag{36a}$$

$$\delta v_0^\eta : \frac{\partial}{R\partial\theta}N_{\theta\theta}^\eta + \frac{2N_{R\theta}^\eta}{R} + \frac{\partial}{\partial R}N_{R\theta}^\eta = I_0^\eta\frac{\partial^2 v_0^\eta}{\partial t^2} + I_1^\eta\frac{\partial^2 v_1^\eta}{\partial t^2}, \tag{36b}$$

$$\delta w^\eta : \frac{\partial S_{RZ}}{\partial R} + \frac{1}{R}\frac{\partial S_{\theta Z}}{\partial \theta} - K_W w + K_P\frac{\partial^2 w}{\partial R^2} + \frac{K_P}{R^2}\frac{\partial^2 w}{\partial \theta^2} = I_0\frac{\partial^2 w}{\partial t^2}, \tag{36c}$$

$$\delta\phi_R^\eta : \frac{\partial M_{RR}}{\partial R} - \frac{M_{\theta\theta}}{R} + \frac{1}{R}\frac{\partial M_{R\theta}}{\partial\theta} - S_{RZ} = I_1\frac{\partial^2 u_0}{\partial t^2} + I_2\frac{\partial^2 \phi_R}{\partial t^2}, \tag{36d}$$

$$\delta\phi_\theta : \frac{\partial}{R\partial\theta}M_{\theta\theta} + \frac{2}{R}M_{R\theta} + \frac{\partial}{\partial R}M_{R\theta} - M_{\theta z} = I_1^\eta\frac{\partial^2 v_0}{\partial t^2} + I_2^\eta\frac{\partial^2 v_1}{\partial t^2}. \tag{36e}$$

Also, general associated boundary conditions can be given by:

$$\delta u^{\eta} = 0 \text{ or } N^{\eta}_{RR}\hat{n}_R + \frac{N^{\eta}_{R\theta}}{R}\hat{n}_\theta = 0 \ , \tag{37a}$$

$$\delta v = 0 \text{ or } N^{\eta}_{R\theta}\hat{n}_R + \frac{N^{\eta}_{\theta\theta}}{R}\hat{n}_\theta = 0 \ , \tag{37b}$$

$$\delta w^{\eta} = 0 \text{ or } \left[S_{RZ} - K_p\frac{\partial w}{\partial R}\right]^{\eta}\hat{n}_R + \left[\frac{S_{\theta Z}}{R} - \frac{K_p}{R}\frac{\partial w}{\partial \theta}\right]^{\eta}\hat{n}_\theta = 0, \tag{37c}$$

$$\delta \phi^{\eta}_R = 0 \text{ or } \left[M_{RR}\right]^{\eta}\hat{n}_R + \left[\frac{M_{R\theta}}{R}\right]^{\eta}\hat{n}_\theta = 0, \tag{37d}$$

$$\delta \phi^{\eta}_\theta = 0 \text{ or } \left[M_{R\theta}\right]^{\eta}\hat{n}_R + \left[\frac{M_{\theta\theta}}{R}\right]^{\eta}\hat{n}_\theta = 0. \tag{37e}$$

It is noted that, based on the compatibility equations (Eq. (28)), the numbers of unknown variables are declined from 15 to 9. So, the total number of unknowns in the face sheets and core is decreased to 9.

2.6 Solution procedure

In this part of the present work, we displayed an FE-based [51, 52] solution procedure which is called GDQM for solving the formulation of the current problem. The first assumption in this is as follows:

$$\left.\frac{\partial f}{\partial r}\right|_{r=r_i,\,\theta=\theta_j} = \sum_{m=1}^{N_r}\sum_{n=1}^{N_\theta} A^r_{im} I^\theta_{jn} f_{mn}, \tag{38a}$$

$$\left.\frac{\partial f}{\partial \theta}\right|_{r=r_i,\,\theta=\theta_j} = \sum_{m=1}^{N_r}\sum_{n=1}^{N_\theta} I^r_{im} A^\theta_{jn} f_{mn}, \tag{38b}$$

$$\frac{\partial}{\partial r}\left(\left.\frac{\partial f}{\partial \theta}\right|_{r=r_i,\,\theta=\theta_j}\right) = \sum_{m=1}^{N_r}\sum_{n=1}^{N_\theta} A^r_{im} A^\theta_{jn} f_{mn}, \tag{38c}$$

$$\left.\frac{\partial^2 f}{\partial r^2}\right|_{r=r_i,\,\theta=\theta_j} = \sum_{m=1}^{N_r}\sum_{n=1}^{N_\theta} B^r_{im} I^\theta_{jn} f_{mn}, \tag{38d}$$

$$\left.\frac{\partial^2 f}{\partial \theta^2}\right|_{r=r_i,\,\theta=\theta_j} = \sum_{m=1}^{N_r}\sum_{n=1}^{N_\theta} I^r_{im} B^\theta_{jn} f_{mn}. \tag{38e}$$

Also, I^r_{im} and I^θ_{jn} are equal to one when i = m and j = n, otherwise are equal to zero. Also, A^r_{im}, A^θ_{jn}, B^r_{im} and B^θ_{jn} are weighting coefficients of the first- and second-order derivatives along with the r and θ directions, respectively, and may be considered as

$$A^r_{im} = \begin{cases} \frac{\xi(r_i)}{(r_i - r_m)\xi(r_m)} & \text{when } i \neq m \\ -\sum\limits_{k=1,k\neq i}^{N_r} A_{ik} & \text{when } i = m \end{cases} \quad i, m = 1, 2, \ldots, N_r, \tag{39a}$$

$$A^\theta_{jn} = \begin{cases} \frac{\xi(\theta_j)}{(\theta_j - \theta_n)\xi(\theta_n)} & \text{when } j \neq n \\ -\sum\limits_{k=1,k\neq j}^{N_\theta} A_{jk} & \text{when } j = n \end{cases} \quad j, n = 1, 2, \ldots, N_\theta, \tag{39b}$$

in which

$$\xi(r_i) = \prod_{k=1,k\neq i}^{N_r} (r_i - r_k), \tag{40a}$$

$$\xi(\theta_j) = \prod_{k=1,k\neq j}^{N_\theta} (\theta_j - \theta_k), \tag{40b}$$

and

$$B^r_{im} = 2\left(A^r_{ii}A^r_{im} - \frac{A^r_{im}}{(r_i - r_m)}\right) \quad i, m = 1, 2, \ldots, N_r \ , \ i \neq m, \tag{41a}$$

$$B^\theta_{jn} = 2\left(A^\theta_{jj}A^\theta_{jn} - \frac{A^\theta_{jn}}{(\theta_j - \theta_n)}\right) \quad j, n = 1, 2, \ldots, N_\theta \ , \ j \neq n, \tag{41b}$$

$$B^r_{ii} = -\sum_{k=1,k\neq i}^{N_r} B^r_{ik} \ , \ i = 1, 2, \ldots, N_r, \ i = m, \tag{41c}$$

$$B^\theta_{jj} = -\sum_{k=1,k\neq j}^{N_\theta} B^\theta_{jk} \ , \ j = 1, 2, \ldots, N_j, \ j = n. \tag{41d}$$

Also, using Chebyshev polynomials greed points, the seed along with the r-axis and θ-axis can be distributed as [98]:

$$r_i = \frac{R_0 - R_i}{2}\left(1 - \cos\left(\frac{(i-1)}{(N_r - 1)}\pi\right)\right) + R_i \quad i = 1, 2, 3, \ldots, N_r, \tag{42a}$$

$$\theta_j = \frac{\chi}{2}\left(1 - \cos\left(\frac{(j-1)}{(N_\theta - 1)}\pi\right)\right) \quad j = 1, 2, 3, \ldots, N_\theta. \tag{42b}$$

The following equation can give the GDQ form of the structure:

$$\left\{\left[\begin{bmatrix}M_{\mathrm{dd}}\\M_{\mathrm{bd}}\end{bmatrix}\begin{bmatrix}M_{\mathrm{db}}\\M_{\mathrm{bb}}\end{bmatrix}\right]\omega_n^2+\left[\begin{bmatrix}K_{\mathrm{dd}}\\K_{\mathrm{bd}}\end{bmatrix}\begin{bmatrix}K_{\mathrm{db}}\\K_{\mathrm{bb}}\end{bmatrix}\right]\right\}\left\{\begin{matrix}\delta_{\mathrm{d}}\\\delta_{\mathrm{b}}\end{matrix}\right\}=0. \tag{43}$$

Finally, with the aid of Eq. (43), the new system is

$$\left[K_{\mathrm{db}}\right]\delta_{\mathrm{b}}+\left[K_{\mathrm{dd}}\right]\delta_{\mathrm{d}}=0, \tag{44a}$$

$$\left[K_{\mathrm{bb}}\right]\delta_{\mathrm{b}}+\left[K_{\mathrm{bd}}\right]\delta_{\mathrm{d}}=0, \tag{44b}$$

where the vector of the freedom degrees can be defined as:

$$\delta_{\mathrm{b}}=-\frac{\left[K_{\mathrm{dd}}\right]}{\left[K_{\mathrm{db}}\right]}\delta_{\mathrm{d}}. \tag{45}$$

By substituting Eq. (45) in Eq. (44b), we have:

$$\left(\left[K_{\mathrm{bd}}\right]-\left[K_{\mathrm{bb}}\right]\left[K_{\mathrm{db}}\right]^{-1}\left[K_{\mathrm{dd}}\right]\right)\delta_{\mathrm{d}}=0. \tag{46}$$

So,

$$K^*=\left[K_{\mathrm{bd}}\right]-\left[K_{\mathrm{bb}}\right]\left[K_{\mathrm{db}}\right]^{-1}\left[K_{\mathrm{dd}}\right] \tag{47}$$

and

$$\left[M_{\mathrm{bd}}\right]\delta_{\mathrm{d}}+\left[M_{\mathrm{bb}}\right]\delta_{\mathrm{b}}=0. \tag{48}$$

Also, by substituting Eqs. (45) in (48), we have:

$$\left(\left[M_{\mathrm{bd}}\right]-\left[M_{\mathrm{bb}}\right]\left[K_{\mathrm{db}}\right]^{-1}\left[K_{\mathrm{dd}}\right]\right)\delta_{\mathrm{d}}=0. \tag{49}$$

So,

$$M^*=\left[M_{\mathrm{bd}}\right]-\left[M_{\mathrm{bb}}\right]\left[K_{\mathrm{db}}\right]^{-1}\left[K_{\mathrm{dd}}\right]. \tag{50}$$

Finally, by solving the below equation, frequency information and displacement fields of the structure can be extracted using GDQM.

$$K^*+M^*\omega^2=0. \tag{51}$$

3 Results and discussion

The data in Table 1 provide details about the properties of the reinforcements and epoxy. The thermomechanical constants of the used reinforcements are given in Table 1. Also, carbon fiber, epoxy, and carbon nanotube are used to make a reinforced sandwich disk with honeycomb core and multiscale hybrid nanocomposite face sheets and core.

Convergence conditions of the GDQ method for having independent outcomes with respect to the three boundary conditions are shown in Table 2. Based on Table 2, when the number of grid points in the GDQ method is more than 11, the error for calculating the natural frequency of the disk becomes zero, and this matter is a fact for all boundary conditions.

The influence of the number of layers (Nt) and various functionally graded distribution on the frequency of the disk with respect to the porosity patterns are depicted in Table 3. If we have a glance at the Table 3 can claim that not only the structure will have the best dynamic response, which is considered the FG-O and PD-X patterns, but also the number of layers should not be more than nine for all porosity and FG patterns, because of that for $Nt \geq 9$ we cannot see any changes in the frequency of the structure.

They analyze the effects of three types of methods for reinforcing the structure on the frequency of the system with consideration of three porosity coefficient and boundary conditions, which are discussed in Table 3. The ends of Table 4 show that not only CNTs/HC/CNTs reinforced disk has the highest natural frequency in comparison with MHC/HC/MHC, but also the imperfection effect is a reason to increase the frequency of the system. If we have a glance at the given information in Table 4, we can conclude that employing the honeycomb network as the core of the structure will improve the dynamic response of the structure impressively.

The provided information in Fig. 5 gives results about the frequency behavior of the disk by considering the angle of the honeycomb network effect. The more critical conclusion

Table 1 The properties of MHC [99] and core [19]

Carbon (fiber)	Epoxy (matrix)	Carbon nanotube	Core (aluminum)
$E^{\mathrm{f}}_{11}(\mathrm{GPa})=233.05$	$v^{\mathrm{m}}=0.34$	$E^{\mathrm{cnt}}(\mathrm{Gpa})=640$	$v^{s}=0.34$
$E^{f}_{11}(\mathrm{GPa})=23.1$	$\rho^{\mathrm{m}}\left(\frac{\mathrm{kg}}{\mathrm{m}^3}\right)=1200$	$d^{\mathrm{cnt}}(\mathrm{m})=1.4\times10^{-9}$	$\rho^{s}\left(\frac{\mathrm{kg}}{\mathrm{m}^3}\right)=2700$
$G^{\mathrm{f}}_{11}(\mathrm{GPa})=8.96$	$E^{\mathrm{m}}(\mathrm{Gpa})=3.51$	$t^{\mathrm{cnt}}(\mathrm{m})=0.34\times10^{-9}$	$E^{\mathrm{s}}(\mathrm{Gpa})=70$
$\upsilon^{\mathrm{f}}=0.2$		$l^{\mathrm{cnt}}(\mathrm{m})=25\times10^{-6}$	
$\rho^{\mathrm{f}}\left(\frac{\mathrm{kg}}{\mathrm{m}^3}\right)=1750$		$\vartheta_{12}=0.33$	
		$\rho^{\mathrm{cnt}}\left(\mathrm{kg}/\mathrm{m}^3\right)=1350$	

in Fig. 5 is that when the angle of the fibers is close to the horizon, the frequency of the system improves.

The provided information in Fig. 6 gives results about the frequency behavior of the disk considering V_f effect. The more important conclusion in Fig. 6 is that when the sandwich disk is made of the higher value fraction of carbon fibers, the frequency of the system could be improved.

The provided information in Fig. 7 gives results about the frequency behavior of the disk considering the value fraction of CNTs (W_{CNT}) effect. The more important conclusion in Fig. 7 is that when the sandwich disk is made of a higher value fraction of CNTs, the frequency of the system could be improved.

The presented diagrams in Fig. 8 give the results about the frequency behavior of the disk considering the thickness to length ratio of the honeycomb network (t_h/l_h) effect. Concerning Fig. 8, the thicker the honeycomb core, the better is the dynamic provided for the sandwich disk.

Figure 9 presents some information for analyzing the impacts of the orientation of fibers (θ_f/π) in the epoxy matrix and thickness to length ratio of the honeycomb network (t_h/l_h) on the vibrational information of a sandwich disk with consideration of three kinds of boundary conditions. The main point in this part of the presented study is that for the structure with C–C and C–S edges and each t_h/l_h, the lowest frequency response is for a disk which is reinforced by the carbon fibers with $\theta_f/\pi=0.5$, and this fiber angle is called the critical angle. Also, for S–S boundary conditions, the critical fiber angles are 0.34 and 0.68. Besides, as the t_h/l_h increases, the frequency of the structure

Table 2 Convergence number of grid points for having independent results with respect to the three kinds of boundary conditions

Boundary conditions	$N=5$	$N=7$	$N=9$	$N=11$	$N=13$	$N=15$
Simply–Simply	0.0350	0.0407	0.0412	0.0413	0.0413	0.0413
Clamped–Simply	0.1001	0.0986	0.0988	0.0988	0.0988	0.0988
Clamped–Clamped	0.1371	0.1355	0.1356	0.1356	0.1356	0.1356

Table 3 Convergence number of layers in the compositionally face sheets and various functionally graded distribution effects on the frequency of the disk with respect to the porosity patterns

PD	CNT-distribution	Nt = 1	Nt = 3	Nt = 5	Nt = 7	Nt = 9	Nt = 11	Nt = 13	Nt = 15	Nt = ∞
X	FG-X	0.1395	0.1373	0.1380	0.1383	0.1384	0.1384	0.1384	0.1385	0.1385
	FG-O	0.1421	0.1364	0.1359	0.1357	0.1357	0.1356	0.1356	0.1356	0.1356
	FG-UD	0.1411	0.1368	0.1368	0.1368	0.1367	0.1367	0.1367	0.1367	0.1368
O	FG-X	0.1257	0.1370	0.1373	0.1373	0.1373	0.1373	0.1373	0.1373	0.1373
	FG-O	0.1296	0.1354	0.1356	0.1356	0.1356	0.1356	0.1356	0.1356	0.1357
	FG-UD	0.1285	0.1359	0.1361	0.1361	0.1361	0.1361	0.1361	0.1361	0.1361
UD	FG-X	0.1335	0.1362	0.1368	0.1369	0.1370	0.1370	0.1371	0.1371	0.1371
	FG-O	0.1367	0.1352	0.1348	0.1348	0.1347	0.1347	0.1347	0.1347	0.1347
	FG-UD	0.1356	0.1356	0.1356	0.1356	0.1356	0.1356	0.1356	0.1356	0.1356

Table 4 Effects of three types of methods for reinforcing the structure on the frequency of the system with consideration of three porosity coefficient and boundary conditions

	Simply–Simply			Clamped–Simply			Clamped–Clamped		
	FG-X	FG-O	FG-UD	FG-X	FG-O	FG-UD	FG-X	FG-O	FG-UD
Without imperfection ($e_0=0$)									
MHC/HC/MHC[a]	0.0398	0.0388	0.0391	0.0952	0.0928	0.0936	0.1306	0.1273	0.1285
CNT/HC/CNT[b]	0.0499	0.0405	0.0475	0.0835	0.0707	0.0795	0.1200	0.1008	0.1165
With imperfection ($e_0=0.2$)									
MHC/HC/MHC[a]	0.0406	0.0396	0.0400	0.0971	0.0948	0.0956	0.1332	0.1301	0.1312
CNT/HC/CNT[b]	0.0461	0.0331	0.0417	0.0785	0.0604	0.0712	0.1150	0.0905	0.1052
With imperfection ($e_0=0.4$)									
MHC/HC/MHC[a]	0.0416	0.0406	0.0410	0.0994	0.0973	0.0981	0.1365	0.1335	0.1347
CNT/HC/CNT[b]	0.0566	0.0417	0.0517	0.0960	0.0742	0.0852	0.1339	0.1052	0.1268

[a]Multiscale hybrid nanocomposite reinforced disk /honeycomb/multiscale hybrid nanocomposite reinforced disk

[b]Carbon nanotubes reinforced disk/honeycomb/ carbon nanotubes reinforced disk

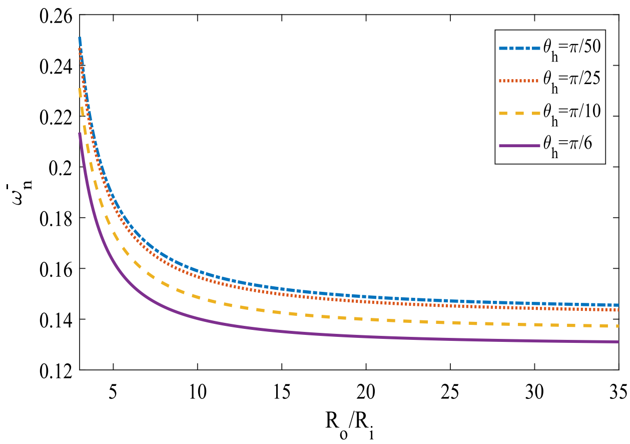

Fig. 5 Frequency of the clamped–clamped honeycomb reinforced disk versus the outer to inner radius ratio for various θ_h

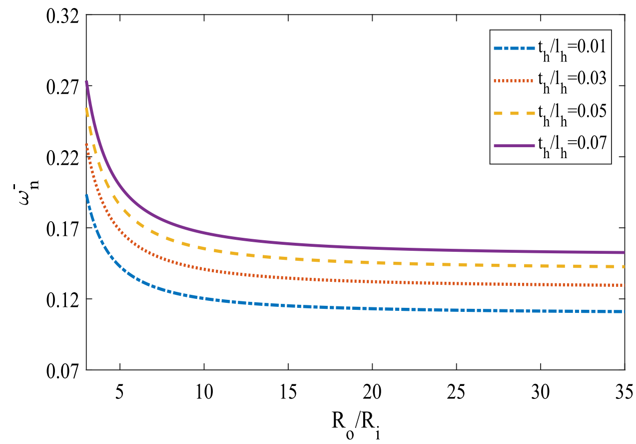

Fig. 8 Frequency of the clamped–clamped honeycomb-reinforced disk versus the radius ratio for various t_h/l_h

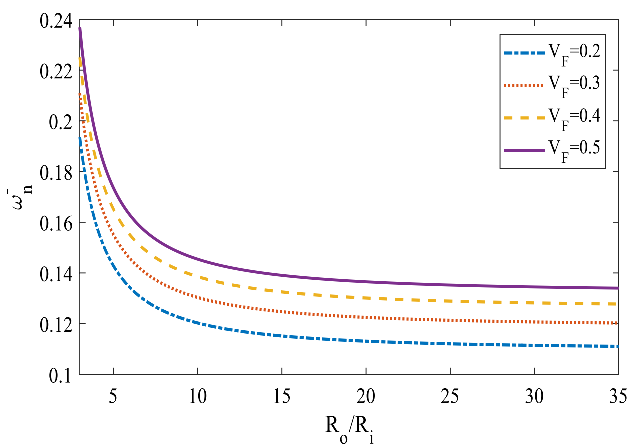

Fig. 6 Frequency of the clamped–clamped honeycomb reinforced disk versus radius ratio for various V_f

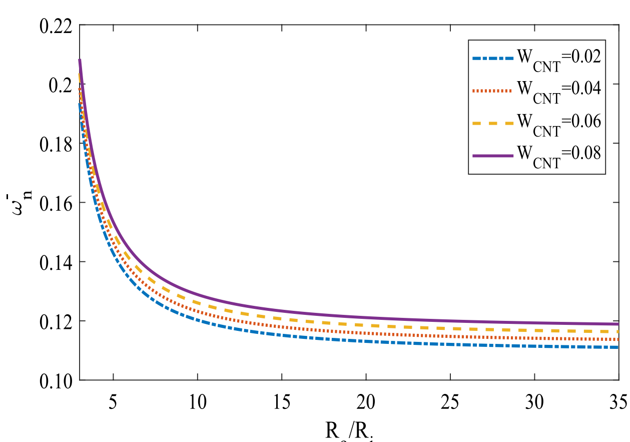

Fig. 7 Frequency of the clamped–clamped honeycomb-reinforced disk versus the radius ratio for various W_{CNT}

with critical fiber angles increases. Furthermore, when there is an ever increase in θ_f/π, before and after critical fiber angles, the dynamic response of the disk increases and falls, respectively. The last result from Fig. 9 is that employing the thicker honeycomb core will enhance the stability of the structure.

Figure 10 presents some data for analyzing the impacts of the orientation of fibers (θ_f/π) in the epoxy matrix, Winkler–Pasternak constants (K_w and K_p), and three kinds of boundary conditions on the vibrational information of a sandwich disk. As K_w and K_p increase, the frequency of the disk increases. In addition, it is true that the roles of K_w and K_p are the same as enhancements, but the impact of K_w could be much more considerable than the effect of K_p on the stability of the structure.

4 Conclusion

For the first time, the vibrational characteristics of a sandwich disk rested on the elastic foundation is investigated. The stresses and strains are obtained using FSDT. Rule of the mixture and modified Halpin–Tsai model are engaged to provide the effective material constant of the multi-hybrid laminated nanocomposite face sheets of the sandwich disk. Finally, the most bolded results of this paper are as follows:

Not only CNTs/HC/CNTs reinforced disk have the highest natural frequency compared with MHC/HC/MHC, but also growing the imperfection effect is a reason to decline the frequency of the systems.

We can conclude that employing the honeycomb network as the core of the structure improves the dynamic response of the design impressively.

When the angle of the fibers is close to the horizon, the frequency of the system improves.

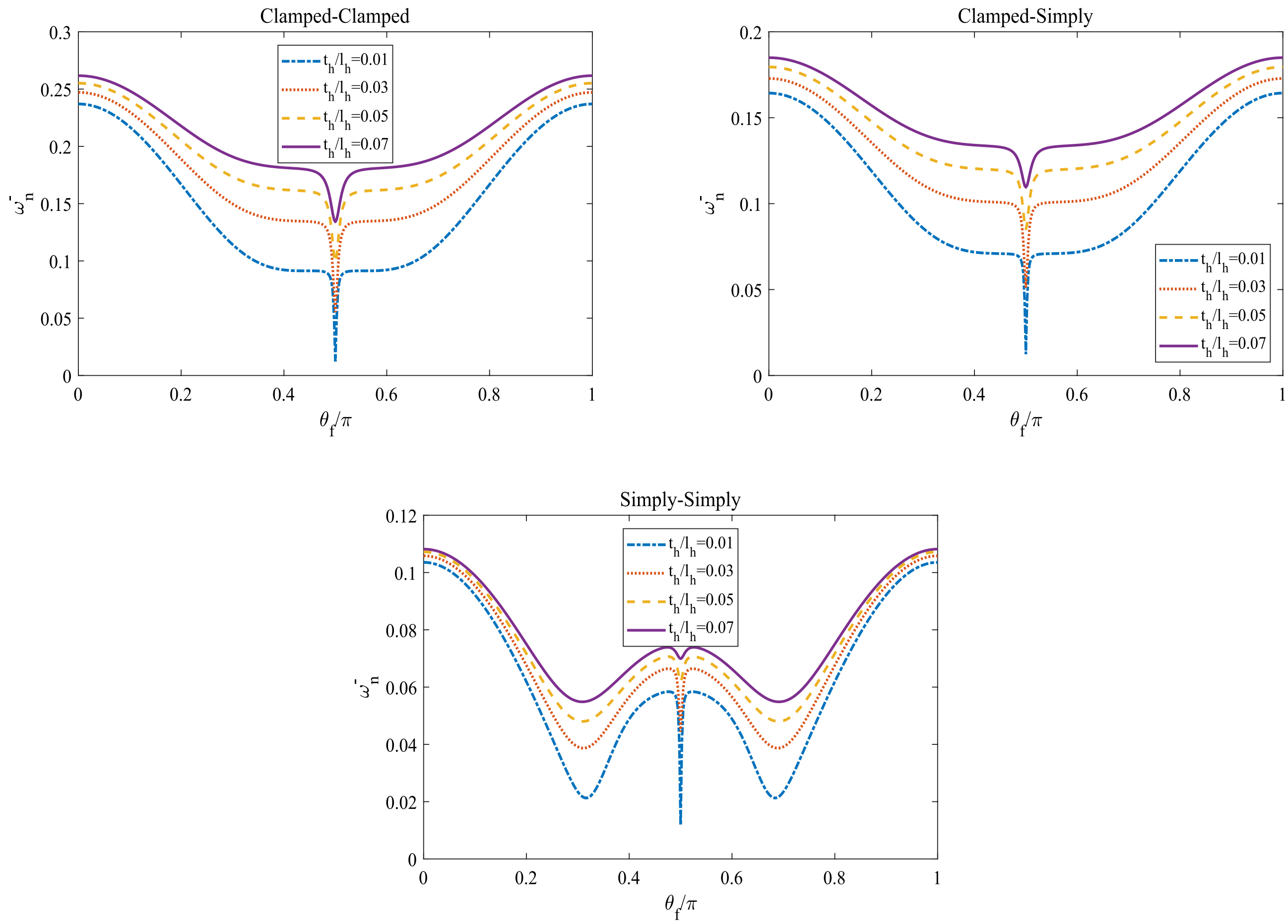

Fig. 9 Frequency of the honeycomb-reinforced disk versus θ_f/π for various t_h/l_h and three kinds of boundary conditions

For the structure with C–C and C–S edges and each value of t_h/l_h, the lowest frequency response is for a disk which is reinforced by the carbon fibers with $\theta_f/\pi = 0.5$, and this fiber angle is called the critical fiber angle.

For S–S boundary conditions, the critical fiber angles are 0.34 and 0.68. Also, as the t_h/l_h increases, the frequency of the structure with critical fiber angles increases.

Funding National Natural Science Foundation of China (51675148). The Outstanding Young Teachers Fund of Hangzhou Dianzi University (GK160203201002/003). National Natural Science Foundation of China (51805475). This research was supported by the 2020 scientific promotion funded by Jeju National University.

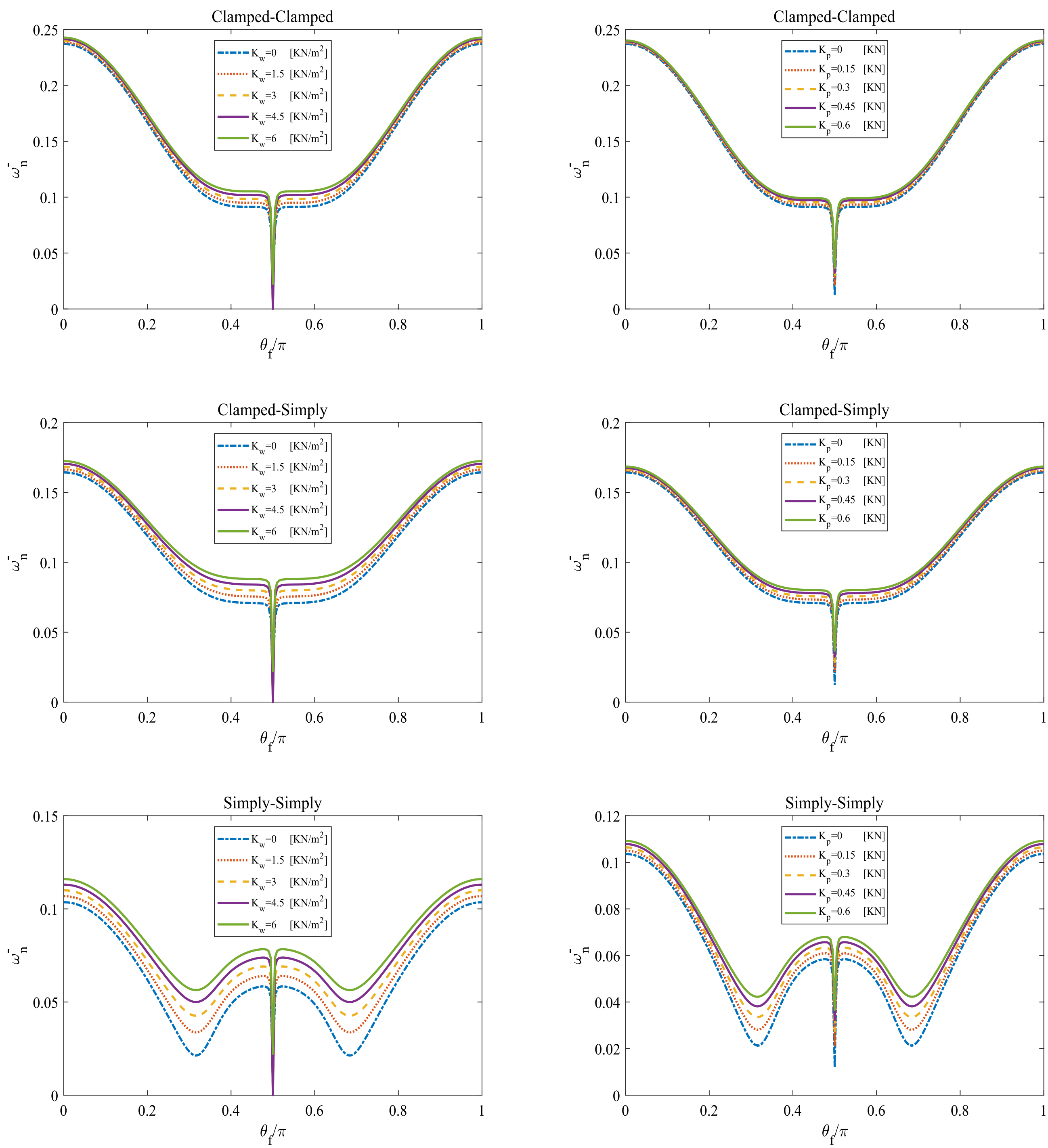

Fig. 10 Frequency of the honeycomb-reinforced disk versus to θ_f/π for three values of K_w and K_p with three kinds of boundary conditions

References

1. Chen S, Wang G, Zuo S, Yang C (2019) Experimental investigation on microstructure and permeability of thermally treated beishan granite. J Test Eval 49(2). https://doi.org/10.1520/JTE20180879.
2. Ye X, Wang S, Zhang S, Xiao X, Xu F (2020) The compaction effect on the performance of a compaction-grouted soil nail in sand. Acta Geotech, pp 1–13. https://doi.org/10.1007/s11440-020-01017-4
3. Sheng D, Zhang S, Yu Z, Zhang J (2013) Assessing frost susceptibility of soils using PCHeave. Cold Reg Sci Technol 95:27–38. https://doi.org/10.1016/j.coldregions.2013.08.003
4. Zhang S, Leng W, Zhang F, Xiong Y (2012) A simple thermo-elastoplastic model for geomaterials. Int J Plast 34:93–113. https://doi.org/10.1016/j.ijplas.2012.01.011
5. Zhang S, Teng J, He Z, Liu Y, Liang S, Yao Y, Sheng D (2016) Canopy effect caused by vapour transfer in covered freezing soils.

Géotechnique 66(11):927–940. https://doi.org/10.1680/jgeot.16.P.016
6. Zghal S, Frikha A, Dammak F (2018) Mechanical buckling analysis of functionally graded power-based and carbon nanotubes-reinforced composite plates and curved panels. Compos B Eng 150:165–183
7. Tornabene F, Liverani A, Caligiana G (2011) FGM and laminated doubly curved shells and panels of revolution with a free-form meridian: a 2-D GDQ solution for free vibrations. Int J Mech Sci 53(6):446–470
8. Frikha A, Zghal S, Dammak F (2018) Dynamic analysis of functionally graded carbon nanotubes-reinforced plate and shell structures using a double directors finite shell element. Aerosp Sci Technol 78:438–451
9. Tornabene F, Reddy J (2013) FGM and laminated doubly-curved and degenerate shells resting on nonlinear elastic foundations: a GDQ solution for static analysis with a posteriori stress and strain recovery. J Indian Inst Sci 93(4):635–688
10. Trabelsi S, Frikha A, Zghal S, Dammak F (2019) A modified FSDT-based four nodes finite shell element for thermal buckling analysis of functionally graded plates and cylindrical shells. Eng Struct 178:444–459
11. Tornabene F, Fantuzzi N, Viola E, Batra RC (2015) Stress and strain recovery for functionally graded free-form and doubly-curved sandwich shells using higher-order equivalent single layer theory. Compos Struct 119:67–89. https://doi.org/10.1016/j.compstruct.2014.08.005
12. Tornabene F, Fantuzzi N, Bacciocchi M, Viola E (2016) Effect of agglomeration on the natural frequencies of functionally graded carbon nanotube-reinforced laminated composite doubly-curved shells. Compos B Eng 89:187–218. https://doi.org/10.1016/j.compositesb.2015.11.016
13. Mukhopadhyay T, Adhikari S (2016) Free-vibration analysis of sandwich panels with randomly irregular honeycomb core. J Eng Mech 142(11):06016008
14. Suryawanshi VJ, Pawar AC, Palekar SP, Rade KA (2020) Defect detection of composite honeycomb structure by vibration analysis technique. In: Materials Today: Proceedings
15. Mozafari H, Najafian S (2019) Vibration analysis of foam filled honeycomb sandwich panel–numerical study. Austral J Mech Eng 17(3):191–198
16. Xu G-d, Zeng T, Cheng S, Wang X-h, Zhang K (2019) Free vibration of composite sandwich beam with graded corrugated lattice core. Compos Struct 229:111466
17. Amini A, Mohammadimehr M, Faraji A (2019) Active control to reduce the vibration amplitude of the solar honeycomb sandwich panels with CNTRC facesheets using piezoelectric patch sensor and actuator. Steel Compos Struct 32(5):671–686
18. Shahverdi H, Barati MR, Hakimelahi B (2019) Post-buckling analysis of honeycomb core sandwich panels with geometrical imperfection and graphene reinforced nano-composite face sheets. Mater Res Express 6(9):095017
19. Sobhy M (2020) Differential quadrature method for magneto-hygrothermal bending of functionally graded graphene/Al sandwich-curved beams with honeycomb core via a new higher-order theory. J Sandw Struct Mater, p 1099636219900668
20. Wang Y-j, Zhang Z-j, Xue X-m, Zhang L (2019) Free vibration analysis of composite sandwich panels with hierarchical honeycomb sandwich core. Thin-Walled Struct 145:106425
21. Zhang Z-j, Han B, Zhang Q-c, Jin F (2017) Free vibration analysis of sandwich beams with honeycomb-corrugation hybrid cores. Compos Struct 171:335–344
22. Zhang Y, Li Y (2019) Nonlinear dynamic analysis of a double curvature honeycomb sandwich shell with simply supported boundaries by the homotopy analysis method. Compos Struct 221:110884
23. Keleshteri M, Asadi H, Aghdam M (2019) Nonlinear bending analysis of FG-CNTRC annular plates with variable thickness on elastic foundation. Thin-Walled Struct 135:453–462
24. Ansari R, Torabi J (2019) Nonlinear free and forced vibration analysis of FG-CNTRC annular sector plates. Polym Compos 40(S2):E1364–E1377
25. Keleshteri M, Asadi H, Wang Q (2017a) Postbuckling analysis of smart FG-CNTRC annular sector plates with surface-bonded piezoelectric layers using generalized differential quadrature method. Comput Methods Appl Mech Eng 325:689–710
26. Mohammadzadeh-Keleshteri M, Asadi H, Aghdam M (2017) Geometrical nonlinear free vibration responses of FG-CNT reinforced composite annular sector plates integrated with piezoelectric layers. Compos Struct 171:100–112
27. Keleshteri M, Asadi H, Wang Q (2017b) Large amplitude vibration of FG-CNT reinforced composite annular plates with integrated piezoelectric layers on elastic foundation. Thin-Walled Struct 120:203–214
28. Torabi J, Ansari R (2017) Nonlinear free vibration analysis of thermally induced FG-CNTRC annular plates: Asymmetric versus axisymmetric study. Comput Methods Appl Mech Eng 324:327–347
29. Zhao X, Li D, Yang B, Ma C, Zhu Y, Chen H (2014) Feature selection based on improved ant colony optimization for online detection of foreign fiber in cotton. Appl Soft Comput 24:585–596
30. Wang M, Chen H (2020) Chaotic multi-swarm whale optimizer boosted support vector machine for medical diagnosis. Applied Soft Computing 88:105946
31. Zhao X, Zhang X, Cai Z, Tian X, Wang X, Huang Y, Chen H, Hu L (2019) Chaos enhanced grey wolf optimization wrapped ELM for diagnosis of paraquat-poisoned patients. Comput Biol Chem 78:481–490
32. Xu X, Chen H-L (2014) Adaptive computational chemotaxis based on field in bacterial foraging optimization. Soft Comput 18(4):797–807
33. Shen L, Chen H, Yu Z, Kang W, Zhang B, Li H, Yang B, Liu D (2016) Evolving support vector machines using fruit fly optimization for medical data classification. Knowl-Based Syst 96:61–75
34. Wang M, Chen H, Yang B, Zhao X, Hu L, Cai Z, Huang H, Tong C (2017) Toward an optimal kernel extreme learning machine using a chaotic moth-flame optimization strategy with applications in medical diagnoses. Neurocomputing 267:69–84
35. Xu Y, Chen H, Luo J, Zhang Q, Jiao S, Zhang X (2019) Enhanced Moth-flame optimizer with mutation strategy for global optimization. Inf Sci 492:181–203
36. Chen H, Zhang Q, Luo J, Xu Y, Zhang X (2020) An enhanced Bacterial Foraging Optimization and its application for training kernel extreme learning machine. Appl Soft Comput 86:105884
37. Vinyas M, Harursampath D (2020) Nonlinear vibrations of magneto-electro-elastic doubly curved shells reinforced with carbon nanotubes. Compos Struct 253:112749
38. Dat ND, Quan TQ, Mahesh V, Duc ND (2020) Analytical solutions for nonlinear magneto-electro-elastic vibration of smart sandwich plate with carbon nanotube reinforced nanocomposite core in hygrothermal environment. Int J Mech Sci 186:105906
39. Mahesh V, Harursampath D (2020) Nonlinear deflection analysis of CNT/magneto-electro-elastic smart shells under multi-physics loading. Mech Based Des Struct Mach, pp 1–25. https://doi.org/10.1080/15376494.2020.1805059
40. Mahesh V, Harursampath D (2020) Nonlinear vibration of functionally graded magneto-electro-elastic higher order plates reinforced by CNTs using FEM. Eng Comput, pp 1–23. https://doi.org/10.1007/s00366-020-01098-5
41. Vinyas M (2020a) On frequency response of porous functionally graded magneto-electro-elastic circular and annular plates with

different electro-magnetic conditions using HSDT. Compos Struct 240:112044
42. Adjerid S, Weinhart T (2009) Discontinuous Galerkin error estimation for linear symmetric hyperbolic systems. Comput Methods Appl Mech Eng 198(37–40):3113–3129
43. Rafiee M, Liu X, He X, Kitipornchai S (2014) Geometrically nonlinear free vibration of shear deformable piezoelectric carbon nanotube/fiber/polymer multiscale laminated composite plates. J Sound Vib 333(14):3236–3251
44. Ghabussi A, Ashrafi N, Shavalipour A, Hosseinpour A, Habibi M, Moayedi H, Babaei B, Safarpour H (2019) Free vibration analysis of an electro-elastic GPLRC cylindrical shell surrounded by viscoelastic foundation using modified length-couple stress parameter. Mech Based Des Struct Mach. https://doi.org/10.1080/15397734.2019.1705166
45. Shokrgozar A, Ghabussi A, Ebrahimi F, Habibi M, Safarpour H (2020) Viscoelastic dynamics and static responses of a graphene nanoplatelets-reinforced composite cylindrical microshell. Mech Based Des Struct Mach. https://doi.org/10.1080/15397734.2020.1719509
46. Shariati A, Ghabussi A, Habibi M, Safarpour H, Safarpour M, Tounsi A, Safa M (2020) Extremely large oscillation and nonlinear frequency of a multi-scale hybrid disk resting on nonlinear elastic foundation. Thin-Walled Struct 154:106840. https://doi.org/10.1016/j.tws.2020.106840
47. Gibson LJ, Ashby MF (1999) Cellular solids: structure and properties. Cambridge University Press, Cambridge
48. Safarpour M, Ghabussi A, Ebrahimi F, Habibi M, Safarpour H (2020) Frequency characteristics of FG-GPLRC viscoelastic thick annular plate with the aid of GDQM. Thin-Walled Struct 150:106683. https://doi.org/10.1016/j.tws.2020.106683
49. Jermsittiparsert K, Ghabussi A, Forooghi A, Shavalipour A, Habibi M, won Jung D, Safa M, (2020) Critical voltage, thermal buckling and frequency characteristics of a thermally affected GPL reinforced composite microdisk covered with piezoelectric actuator. Mech Based Des Struct Mach. https://doi.org/10.1080/15397734.2020.1748052
50. Ghabussi A, Habibi M, NoormohammadiArani O, Shavalipour A, Moayedi H, Safarpour H (2020) Frequency characteristics of a viscoelastic graphene nanoplatelet–reinforced composite circular microplate. J Vib Control, p 1077546320923930. https://doi.org/10.1177/1077546320923930
51. Moayedi H, Darabi R, Ghabussi A, Habibi M, Foong LK (2020) Weld orientation effects on the formability of tailor welded thin steel sheets. Thin-Walled Struct 149:106669. https://doi.org/10.1016/j.tws.2020.106669
52. Ghabussi A, Marnani JA, Rohanimanesh MS (2020) Improving seismic performance of portal frame structures with steel curved dampers. In: Structures, vol 24. Elsevier, pp 27–40. https://doi.org/10.1016/j.istruc.2019.12.025
53. Al-Furjan MSH, Habibi M, Dw J, Sadeghi S, Safarpour H, Tounsi A, Chen G (2020) A computational framework for propagated waves in a sandwich doubly curved nanocomposite panel. Eng Comput. https://doi.org/10.1007/s00366-020-01130-8
54. Al-Furjan M, Habibi M, Chen G, Safarpour H, Safarpour M, Tounsi A (2020a) Chaotic oscillation of a multi-scale hybrid nano-composites reinforced disk under harmonic excitation via GDQM. Compos Struct. https://doi.org/10.1016/j.compstruct.2020.112737
55. Li J, Tang F, Habibi M (2020) Bi-directional thermal buckling and resonance frequency characteristics of a GNP-reinforced composite nanostructure. Eng Comput. https://doi.org/10.1007/s00366-020-01110-y
56. Habibi M, Hashemi R, Sadeghi E, Fazaeli A, Ghazanfari A, Lashini H (2016) Enhancing the mechanical properties and formability of low carbon steel with dual-phase microstructures. J Mater Eng Perform 25(2):382–389
57. Habibi M, Hashemi R, Tafti MF, Assempour A (2018) Experimental investigation of mechanical properties, formability and forming limit diagrams for tailor-welded blanks produced by friction stir welding. J Manuf Process 31:310–323
58. Al-Furjan M, Habibi M, Safarpour H (2020) Vibration control of a smart shell reinforced by graphene nanoplatelets. Int J Appl Mech. https://doi.org/10.1142/S1758825120500660
59. Liu Z, Su S, Xi D, Habibi M (2020) Vibrational responses of a MHC viscoelastic thick annular plate in thermal environment using GDQ method. Mech Based Des Struct Mach, pp 1–26. https://doi.org/10.1080/15397734.2020.1784201
60. Shi X, Li J, Habibi M (2020) On the statics and dynamics of an electro-thermo-mechanically porous GPLRC nanoshell conveying fluid flow. Mech Based Des Struct Mach, pp 1–37. https://doi.org/10.1080/15397734.2020.1772088
61. Habibi M, Safarpour M, Safarpour H (2020) Vibrational characteristics of a FG-GPLRC viscoelastic thick annular plate using fourth-order Runge-Kutta and GDQ methods. Mech Based Des Struct Mach. https://doi.org/10.1080/15397734.2020.1779086
62. Al-Furjan M, Safarpour H, Habibi M, Safarpour M, Tounsi A (2020) A comprehensive computational approach for nonlinear thermal instability of the electrically FG-GPLRC disk based on GDQ method. Eng Comput. https://doi.org/10.1007/s00366-020-01088-7
63. Zhang X, Shamsodin M, Wang H, NoormohammadiArani O, khan AM, Habibi M, Al-Furjan M (2020) Dynamic information of the time-dependent tobullian biomolecular structure using a high-accuracy size-dependent theory. J Biomol Struct Dyn (just-accepted), pp 1–26. https://doi.org/10.1080/07391102.2020.1760939
64. Habibi M, Taghdir A, Safarpour H (2019) Stability analysis of an electrically cylindrical nanoshell reinforced with graphene nanoplatelets. Compos B Eng 175:107125
65. Pourjabari A, Hajilak ZE, Mohammadi A, Habibi M, Safarpour H (2019) Effect of porosity on free and forced vibration characteristics of the GPL reinforcement composite nanostructures. Comput Math Appl 77(10):2608–2626
66. Cheshmeh E, Karbon M, Eyvazian A, Jung D, Tran T, Habibi M, Safarpour M (2020) Buckling and vibration analysis of FG-CNTRC plate subjected to thermo-mechanical load based on higher-order shear deformation theory. Mech Based Des Struct Mach. https://doi.org/10.1080/15397734.2020.1744005
67. Najaafi N, Jamali M, Habibi M, Sadeghi S, Dw J, Nabipour N (2020) Dynamic instability responses of the substructure living biological cells in the cytoplasm environment using stress-strain size-dependent theory. J Biomol Struct Dyn. https://doi.org/10.1080/07391102.2020.1751297
68. Shariati A, Mohammad-Sedighi H, Żur KK, Habibi M, Safa M (2020a) Stability and dynamics of viscoelastic moving rayleigh beams with an asymmetrical distribution of material parameters. Symmetry 12(4):586
69. Oyarhossein MA, Aa A, Habibi M, Makkiabadi M, Daman M, Safarpour H, Jung DW (2020) Dynamic response of the nonlocal strain-stress gradient in laminated polymer composites microtubes. Sci Rep 10(1):5616. https://doi.org/10.1038/s41598-020-61855-w
70. Shamsaddini Lori E, Ebrahimi F, Elianddy Bin Supeni E, Habibi M, Safarpour H (2020) The critical voltage of a GPL-reinforced composite microdisk covered with piezoelectric layer. Eng Comput. https://doi.org/10.1007/s00366-020-01004-z
71. Moayedi H, Ebrahimi F, Habibi M, Safarpour H, Foong LK (2020) Application of nonlocal strain–stress gradient theory and GDQEM for thermo-vibration responses of a laminated composite

nanoshell. Eng Comput. https://doi.org/10.1007/s00366-020-01002-1
72. Safarpour M, Ebrahimi F, Habibi M, Safarpour H (2020) On the nonlinear dynamics of a multi-scale hybrid nanocomposite disk. Eng Comput. https://doi.org/10.1007/s00366-020-00949-5
73. Ebrahimi F, Supeni EEB, Habibi M, Safarpour H (2020) Frequency characteristics of a GPL-reinforced composite microdisk coupled with a piezoelectric layer. Eur Phys J Plus 135(2):144. https://doi.org/10.1140/epjp/s13360-020-00217-x
74. Ebrahimi F, Hashemabadi D, Habibi M, Safarpour H (2019) Thermal buckling and forced vibration characteristics of a porous GNP reinforced nanocomposite cylindrical shell. Microsyst Technol, pp 1–13
75. Adamian A, Safari KH, Sheikholeslami M, Habibi M, Al-Furjan M, Chen G (2020) Critical temperature and frequency characteristics of GPLs-reinforced composite doubly curved panel. Appl Sci 10(9):3251
76. Shariati A, Habibi M, Tounsi A, Safarpour H, Safa M (2020) Application of exact continuum size-dependent theory for stability and frequency analysis of a curved cantilevered microtubule by considering viscoelastic properties. Eng Comput. https://doi.org/10.1007/s00366-020-01024-9
77. Al-Furjan M, Mohammadgholiha M, Alarifi IM, Habibi M, Safarpour H (2020) On the phase velocity simulation of the multi curved viscoelastic system via an exact solution framework. Eng Comput. https://doi.org/10.1007/s00366-020-01152-2
78. Al-Furjan M, Habibi M, Chen G, Safarpour H, Safarpour M, Tounsi A (2020b) Chaotic simulation of the multi-phase reinforced thermo-elastic disk using GDQM. Eng Comput. https://doi.org/10.1007/s00366-020-01144-2
79. Al-Furjan M, Habibi M, won Jung D, Chen G, Safarpour M, Safarpour H, (2020) Chaotic responses and nonlinear dynamics of the graphene nanoplatelets reinforced doubly-curved panel. Eur J Mech A/Solids: https://doi.org/10.1016/j.euromechsol.2020.104091
80. Al-Furjan M, Habibi M, Won Jung D, Sadeghi S, Safarpour H, Tounsi A, Chen G (2020) A computational framework for propagated waves in a sandwich doubly curved nanocomposite panel. Eng Comput, https://doi.org/10.1007/s00366-020-01130-8
81. Al-Furjan M, Oyarhossein MA, Habibi M, Safarpour H, Jung DW (2020) Wave propagation simulation in an electrically open shell reinforced with multi-phase nanocomposites. Eng Comput, pp 1–17. https://doi.org/10.1007/s00366-020-01167-9
82. Al-Furjan M, Oyarhossein MA, Habibi M, Safarpour H, Jung DW, Tounsi A (2020) On the wave propagation of the multi-scale hybrid nanocomposite doubly curved viscoelastic panel. Compos Struct 255:112947. https://doi.org/10.1016/j.compstruct.2020.112947
83. Al-Furjan M, Fereidouni M, Habibi M, Abd Ali R, Ni J, Safarpour M (2020) Influence of in-plane loading on the vibrations of the fully symmetric mechanical systems via dynamic simulation and generalized differential quadrature framework. Eng Comput, pp 1–23. https://doi.org/10.1007/s00366-020-01177-7
84. Li Y, Li S, Guo K, Fang X, Habibi M (2020) On the modeling of bending responses of graphene-reinforced higher order annular plate via two-dimensional continuum mechanics approach. Eng Comput, pp 1–22. https://doi.org/10.1007/s00366-020-01166-w
85. Shariati A, Mohammad-Sedighi H, Żur KK, Habibi M, Safa M (2020b) On the vibrations and stability of moving viscoelastic axially functionally graded nanobeams. Materials 13(7):1707
86. Moayedi H, Habibi M, Safarpour H, Safarpour M, Foong L (2019) Buckling and frequency responses of a graphen nanoplatelet reinforced composite microdisk. Int J Appl Mecha. https://doi.org/10.1142/S1758825119501023
87. Moayedi H, Aliakbarlou H, Jebeli M, Noormohammadiarani O, Habibi M, Safarpour H, Foong L (2020) Thermal buckling responses of a graphene reinforced composite micropanel structure. Int J Appl Mech 12(01):2050010. https://doi.org/10.1142/S1758825120500106
88. Shokrgozar A, Safarpour H, Habibi M (2020) Influence of system parameters on buckling and frequency analysis of a spinning cantilever cylindrical 3D shell coupled with piezoelectric actuator. Proc Inst Mech Eng Part C: J Mech Eng Sci 234(2):512–529
89. Habibi M, Mohammadi A, Safarpour H, Ghadiri M (2019) Effect of porosity on buckling and vibrational characteristics of the imperfect GPLRC composite nanoshell. Mech Based Des Struct Mach, pp 1–30. https://doi.org/10.1080/15397734.2019.1701490
90. Habibi M, Mohammadi A, Safarpour H, Shavalipour A, Ghadiri M (2019) Wave propagation analysis of the laminated cylindrical nanoshell coupled with a piezoelectric actuator. Mech Based Des Struct Mach. https://doi.org/10.1080/15397734.2019.1697932
91. Vinyas M, Harursampath D, Kattimani S (2020) On vibration analysis of functionally graded carbon nanotube reinforced magneto-electro-elastic plates with different electro-magnetic conditions using higher order finite element methods. Defence Technol https://doi.org/10.1016/j.dt.2020.03.012
92. Vinyas M, Harursampath D, Kattimani S (2020) Thermal response analysis of multi-layered magneto-electro-thermo-elastic plates using higher order shear deformation theory. Struct Eng Mech 73(6):667–684
93. Vinyas M, Sandeep A, Nguyen-Thoi T, Ebrahimi F, Duc D (2019) A finite element–based assessment of free vibration behaviour of circular and annular magneto-electro-elastic plates using higher order shear deformation theory. J Intell Mater Syst Struct 30(16):2478–2501
94. Qaderi S, Ebrahimi F, Vinyas M (2019) Dynamic analysis of multi-layered composite beams reinforced with graphene platelets resting on two-parameter viscoelastic foundation. Eur Phys J Plus 134(7):339
95. Vinyas M, Harursampath D (2020) Computational evaluation of electro-magnetic circuits' effect on the coupled response of multifunctional magneto-electro-elastic composites plates exposed to hygrothermal fields. Proc Inst Mech Eng Part C J Mech Eng Sci. https://doi.org/10.1177/0954406220954485
96. Vinyas M (2020b) Interphase effect on the controlled frequency response of three-phase smart magneto-electro-elastic plates embedded with active constrained layer damping: FE study. Mater Res Express 6(12):125707
97. Vinyas M (2019) Vibration control of skew magneto-electro-elastic plates using active constrained layer damping. Compos Struct 208:600–617
98. Tornabene F, Fantuzzi N, Ubertini F, Viola E (2015) Strong formulation finite element method based on differential quadrature: a survey. Appl Mech Rev 10(1115/1):4028859
99. Karimiasl M, Ebrahimi F, Akgöz B (2019) Buckling and post-buckling responses of smart doubly curved composite shallow shells embedded in SMA fiber under hygro-thermal loading. Compos Struct 223:110988

Publisher's Note Springer Nature remains neutral with regard to jurisdictional claims in published maps and institutional affiliations.